# Characterization of Langmuir-Blodgett Films by Electron Spin Resonance Spectroscopy

by

Nairong Hou

A thesis
presented to the University of Waterloo
in fulfillment of the
thesis requirement for the degree of
Master of Science
in
Chemistry (Nanotechnology)

Waterloo, Ontario, Canada, 2019

I hereby declare that I am the sole author of this thesis. This is a true copy of the thesis, including any required final revisions, as accepted by my examiners.

I understand that my thesis may be made electronically available to the public.

**Abstract**

Langmuir-Blodgett (LB) films built up with amphiphilic molecules have well-known optical, electrical and magnetic properties. For most applications, it is fundamentally important to understand the structure of the films. Electron spin resonance (ESR) spectroscopy has proven to be a powerful tool for measuring sample structure, yet few studies have been performed on monolayer LB films, primarily due to a lack of sufficient sensitivity.

In this work, the fabrication and structural characterization of novel spin-labeled LB films is discussed and demonstrated. Mixed 16-DSA/SA monolayer films containing $10^{13} - 10^{14}$ free-radical electron spins were created and characterized for the first-time using continuous wave (CW) ESR spectroscopy and atomic force microscopy (AFM). Through simulation and image analysis, an order parameter was extracted suggesting that the sample assumes a multi-domain liquid crystal structure when deposited on a solid substrate.

**Acknowledgements**

I would like to thank my supervisor, Professor David Cory, for providing me the great opportunity to study in his lab and for giving me the choice to work on my current project. With his guidance and help, I was introduced to the enchanting fields of spin-based quantum information processing and magnetic resonance.

I would also like to thank many members of Professor Cory's group for their friendship, their engaging attitude and patient help, and their inspiring ideas in a variety of different aspects of research. Particularly, I would like to acknowledge Troy Borneman, Madelaine Liddy, Dmitry Akhmetzyanov, Rahul Deshpande, and Guanru Feng who directly assisted me with this project on understanding the project, training of the techniques, and developing the research skills. I have received enormous help especially from Troy, who has been so supportive throughout this whole time and helped me edit this thesis over and over again. It has always been cheerful to work in this lab having George, Peter, and Alex around. Also, many thanks to Carly and Sarah for their kind assistance. Additionally, I would like to thank Professor Jonathan Baugh and Professor Raffi Budakian for their acceptance to be in my committee.

Finally, special thanks to my parents and friends. It would have been impossible for me to go this far without their trust and support.

## Dedication

This is dedicated to my family.

# Table of Contents

# List of Tables

# List of Figures

# Chapter 1

# Introduction

The Langmuir-Blodgett (LB) technique has been commonly employed as a tool for obtaining one molecule thick monolayers [5]. The unique optical, electrical, and magnetic properties of LB films have attracted wide interest in many potential applications, including the construction of chemical sensors and electrochemical devices [4, 13]. LB films also have a potential as a platform for multi-node quantum information processing [3]. For all applications, it is fundamentally important to understand the ordering and orientation of molecules deposited on solid surfaces. Electron spin resonance (ESR) spectroscopy is a powerful tool for such microscopic analysis [4, 7, 11, 31, 26, 27, 13, 14].

## 1.1 Langmuir-Blodgett Films

The Langmuir-Blodgett technique allows convenient, controllable molecular monolayer deposition by passing a solid substrate through a floating monolayer of amphiphilic molecules at the air-water interface [5]. An amphiphile consists of a water soluble hydrophilic head and a water insoluble hydrophobic tail, and it accumulates at the air-water interface as a result of minimizing the system free energy when lowering the surface tension of water. Langmuir films assembled by these molecules are typically one molecule thick, with the hydrophilic end immersed in the water and the hydrophobic end out of the water pointing towards the air [5]. An example of an amphiphilic substance is a fatty acid, which has a polar head group that is hydrophilic and a long saturated or unsaturated hydrocarbon chain that is hydrophobic (figure 1.1). The water solubility of a fatty acid decreases with increasing hydrocarbon chain length. For the build-up of a floating monolayer, there should

be more than 12 hydrocarbons in the chain since a shorter chain leads to the formation of insoluble micelles [20, 17].

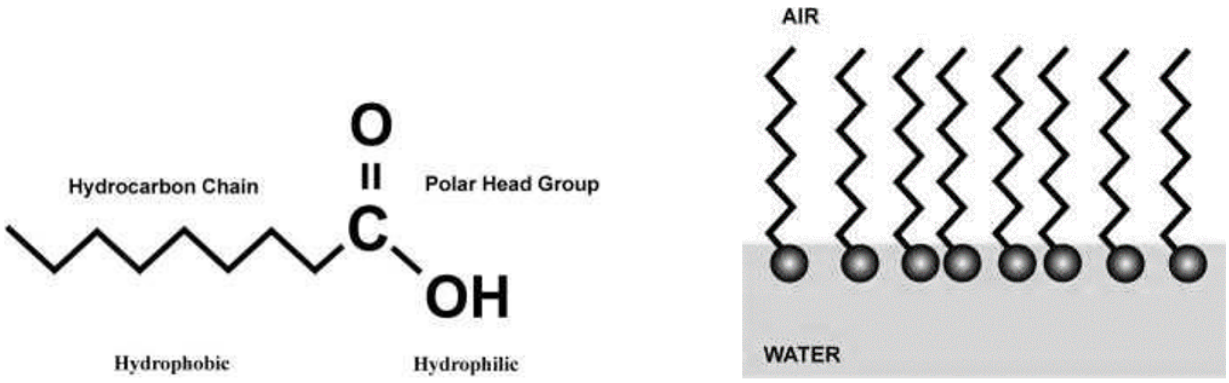


(a) (b)

Figure 1.1: (a) Schematic structure of a fatty acid molecule; (b) Schematic of an insoluble monolayer at the air/water interface [17].

Although various techniques enable the growth of thin organic films - including thermal evaporation, sputtering, electrodeposition, molecular beam epitaxy, and absorption from solution - the LB technique stands out as one of the most promising methods due to precise control of the monolayer thickness and deposition homogeneity over large substrate areas [17].

## 1.2 Electron Spin Resonance Spectroscopy

ESR spectroscopy is a technique that can detect paramagnetic species due to the presence of unpaired electrons in a material [9]. It is useful for revealing conformational structure, dynamic properties, and electronic behavior of organized monolayers [25]. There are two major types of ESR spectrometer: continuous wave (CW) ESR, and pulsed ESR. In the past, CW ESR has been more commonly used for the characterization of LB films that contain unpaired electrons. As shown in figure 1.2, the basic experimental setup of a CW ESR system includes a cavity, a microwave synthesizer, a sweepable magnet, a field modulation system, and a receiver unit for phase sensitive detection [9].

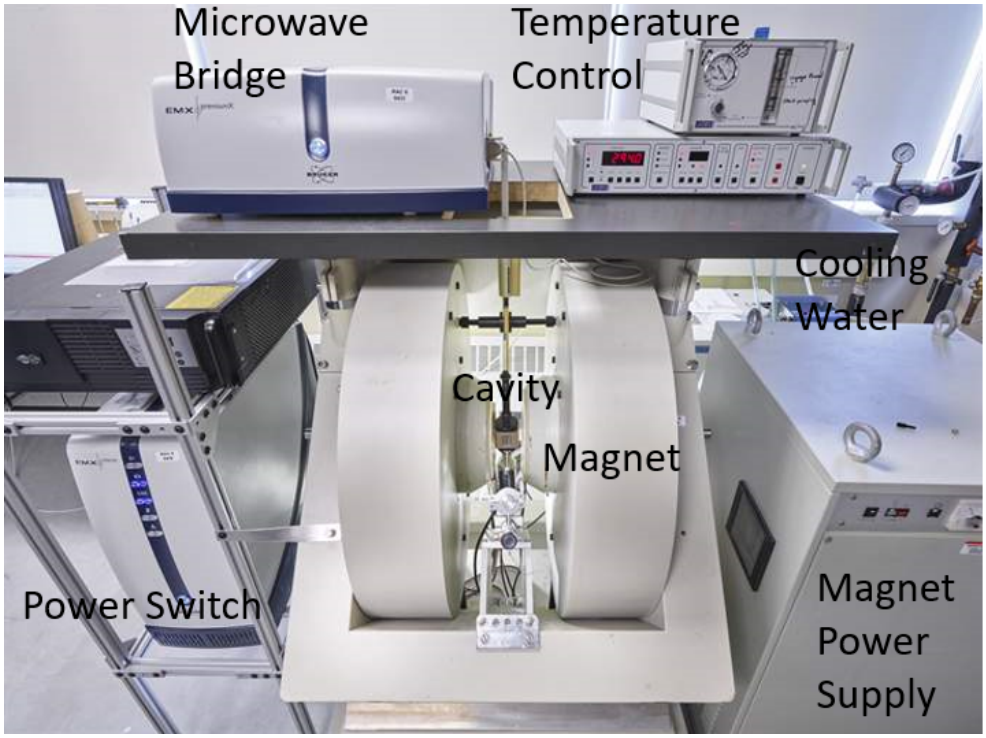


(a)

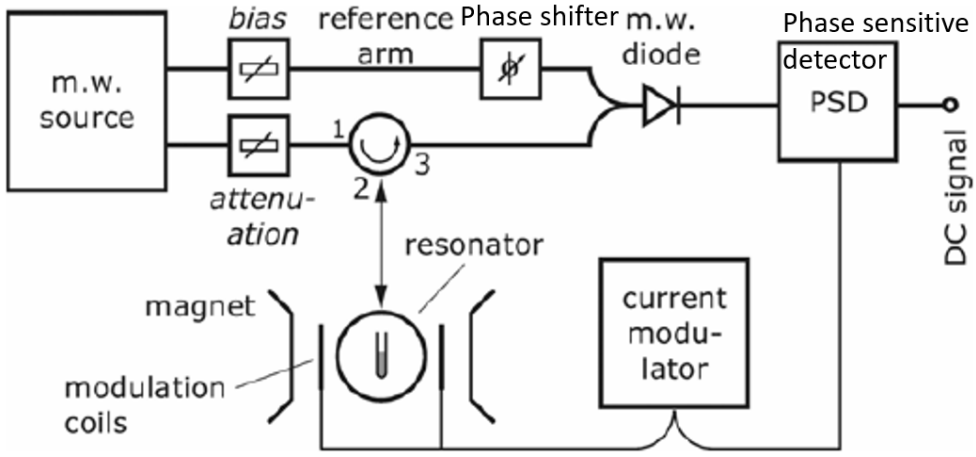


(b)

Figure 1.2: (a)Bruker EMX X-band ESR spectrometer [34]; (b)High-level schematic of a CW ESR spectrometer [8].

The resonator, which is often referred to as the cavity, contains the sample cell and generates a microwave magnetic field at the sample position to both drive spin transitions and efficiently convert the spin response into a detectable microwave signal. The measured line-shape of a sample gives information about molecular orientation through g-value and hyperfine anisotropy [1]. The standard size of a Bruker rectangular parallelepiped TE102 cavity operating at 9.6GHz is $1cm \times 2.25cm \times 4.5cm$ [22], and Bruker EMX spectrometer is equipped with a cylindrical TE011 cavity. An adjustable iris is used to control the coupling of microwaves into the cavity by matching the impedance of the cavity and the waveguide so that signal reflection is minimum when the spin sample is off-resonance. The source output frequency is locked to the resonator center frequency for optimal energy transfer to and from the resonator using an automatic frequency control (AFC) system. The cavity is characterized by a quality factor $Q$ that parameterizes the sharpness of the Lorentzian cavity frequency response, defined as

$$Q = \frac{2\pi(energy\ stored)}{energy\ dissipated\ per\ cycle} = \frac{\nu_{res}}{\Delta\nu}$$

where $\nu_{res}$ is the cavity resonant frequency, and $\Delta\nu$ is the width of the resonance line at half max. When a spin sample is brought on resonance, it absorbs microwave energy and the $Q$ is lowered. The cavity is thus no longer critically coupled due to the change of the $Q$-dependent cavity impedance, and an ESR signal is generated when microwaves are reflected back to the bridge. [9]

Monochromatic microwaves generated by a synthesizer are transmitted to and from the cavity resonator using a waveguide. To couple the source to the resonator, an isolator, attenuator, circulator are used. The isolator minimizes reflections of microwave energy from the system to the source to avoid perturbation. The attenuator is employed to adjust the microwave power level incident on the sample. The microwave power to the cavity and to the detector reflected from the cavity are directed by the circulator. [9]

In practice, the detection of CW microwave absorption by a paramagnetic sample is achieved by fixing the microwave frequency and varying the magnetic field. A small amplitude field modulation is commonly applied to increase signal-to-noise ratio (SNR) by allowing phase-sensitive lock-in detection at an intermediate frequency (normally 100kHz) to suppress low frequency noise. The first-derivative is usually recorded for better resolution, as shown in figure 1.3 [23]. The detected signal intensity increases with larger modulation, but the modulation amplitude should be considerably smaller than the linewidths of the ESR signal to avoid distortion. A low pass filter with variable time constant is used to further improve the sensitivity by filtering out high-frequency noise components. The noise levels drop with increased time constant, but a slower scan rate is needed for

a large time constant to avoid distorting the spin signal. Normally, the time required to scan through the narrowest ESR line should be at least ten times greater than the chosen time constant. [9]

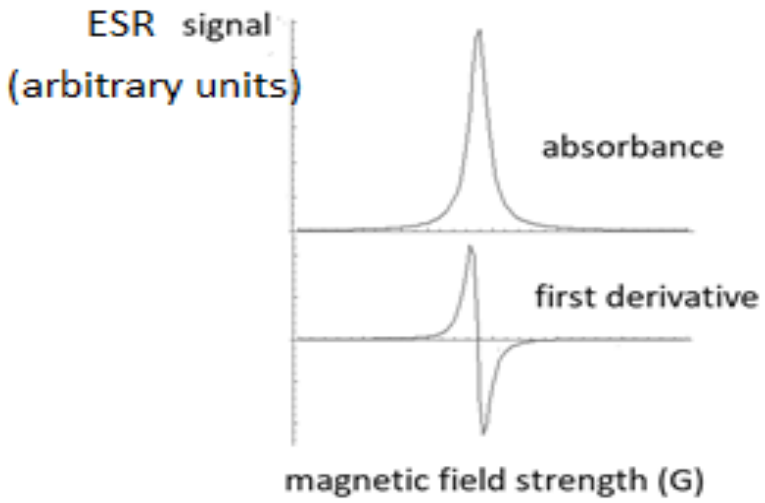


Figure 1.3: ESR absorption line and its first derivative

## 1.3 Atomic Force Microscopy

AFM is a kind of scanning probe microscopy that is frequently used for studying material surface topography with nanometer size resolution by measuring the force between atoms on a probe tip and sample atoms. There is a piezoelectric stack in the scanner, which expands or contracts when a voltage potential is applied, that can resolve small movements to enable precise control of scanning. The position of the probe is detected using an optical lever, and the laser beam is aimed onto the cantilever probe and reflected onto a position sensitive detector. The AFM setup is placed in an acoustic box (figure 1.4) that is closed during measurement. [12]

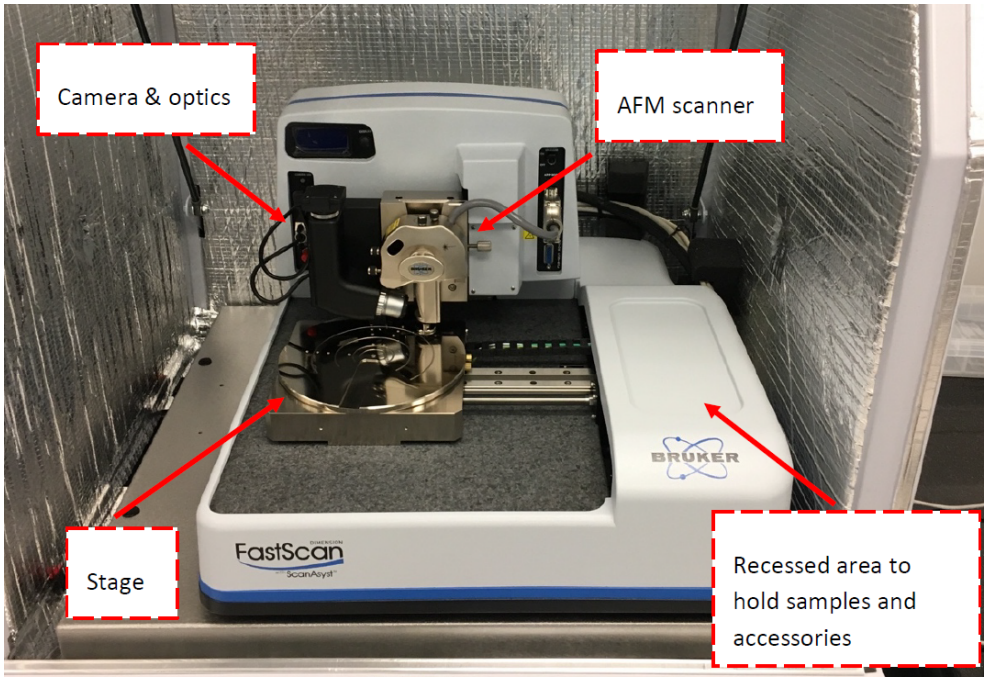


Figure 1.4: Bruker FastScan AFM located at Quantum-Nano Fabrication and Characterization Facility (QNFCF).

## 1.4 Outline

The goal of this thesis is to explore the structure and quality of monolayer LB films containing unpaired electrons through CW ESR and AFM characterization. The ESR spectrum of an LB film contains anisotropy and is orientation dependent. An order parameter can be defined that describes the average alignment of the sample and can be calculated from spectral features, such as peak splittings due to hyperfine coupling. ESR characterization is used extensively for bulk 3D samples, but has not been commonly used for monolayer LB films due to limited sensitivity of most conventional ESR systems.

First, a brief introduction to the LB technique and the ESR technique is given. In the next chapter, the physical principle of the ESR spectrometer is explained. In chapter 3, the fabrication process of monolayer LB films is described. In chapter 4, CW ESR and AFM measurements are shown, along with calculations for the order parameter. Conclusions and future work are discussed in chapter 5.

# Chapter 2

# Basic Principles of CW ESR

Investigation of molecular structure with ESR is based on analyzing the shape and features of the absorption spectrum of electromagnetic radiation by molecules containing unpaired electrons in a magnetic field. Molecules possessing a magnetic-dipole moment interact with the oscillating magnetic component of electromagnetic radiation. This magnetic-dipole moment can arise either from electronic angular momenta of unpaired electrons or nuclear angular momenta of magnetic nuclei. ESR detects the interaction between electromagnetic radiation and electron magnetic moments arising from unpaired electron spins [9]. The quantization of spin angular momentum is an essential step in ESR analysis and can be described by a spin Hamiltonian determined by the interactions between unpaired electrons and their environment. Since LB films are anisotropic systems, the Hamiltonian depends on the orientation of the sample relative to the applied magnetic field. Thus, measuring the orientation-dependent spectrum allows the determination of the sample ordering.

## 2.1 Zeeman Interaction

The quantization of spin angular momentum employs a spin operator that operates on a function to describe a spin state. The electron spin angular momentum operator is commonly notated as a vector $S$ with the nuclear spin operator commonly notated as $I$.

$$S_x = \frac{\hbar}{2}\begin{vmatrix} 0 & 1 \\ 1 & 0 \end{vmatrix}, S_y = \frac{\hbar}{2}\begin{vmatrix} 0 & -i \\ i & 0 \end{vmatrix}, S_z = \frac{\hbar}{2}\begin{vmatrix} 1 & 0 \\ 0 & -1 \end{vmatrix}$$

$$I_x = \frac{\hbar}{\sqrt{2}}\begin{vmatrix} 0 & 1 & 0 \\ 1 & 0 & 1 \\ 0 & 1 & 0 \end{vmatrix}, I_y = \frac{\hbar}{\sqrt{2}}\begin{vmatrix} 0 & -i & 0 \\ i & 0 & -i \\ 0 & i & 0 \end{vmatrix}, I_z = \hbar\begin{vmatrix} 1 & 0 & 0 \\ 0 & 0 & 0 \\ 0 & 0 & -1 \end{vmatrix}$$

For free electrons in a magnetic field, $B$, applied along a direction $z$, the electron-spin magnetic moment along $z$ is

$$\mu_z = \gamma_e \hbar M_S = -g_e \beta_e M_S$$

Here $\hbar$ is the reduced Planck constant, and $M_S$ is the spin angular momentum quantum number. The proportionality constant $\gamma$ is the gyromagnetic ratio that converts angular momentum to magnetic moment. More generally, $\gamma = \frac{gq}{2m}$ for a particle with mass $m$ and charge $q$, where $g$ is the Zeeman factor. The magnitude of associated magnetic moment, $\beta_e \equiv \frac{|e|\hbar}{2m_e}$, is called the Bohr magneton, where $e$ is the electronic charge. The free-electron Zeeman factor $g_e$ is reported to be a value close to 2.0023, giving $\gamma \approx 2.8$MHz/G. [9]

The magnetic energy corresponding to the magnet moment is

$$U = g_e \beta_e B M_S$$

The possible values of $M_S$ for a single unpaired electron are $+\frac{1}{2}$ and $-\frac{1}{2}$, and thus the allowed electronic Zeeman energies $U$ are $\pm\frac{1}{2} g_e \beta_e B$. Spin components of two electrons occupying the same orbital always have opposite signs, so the net magnetic moment of paired electrons in a filled orbital is zero. This separation of energy levels is referred to as Zeeman splitting, given by

$$\Delta U = U_{upper} - U_{lower} = g_e \beta_e B = \gamma_e \hbar B$$

Transitions between the two electronic Zeeman levels can occur when the incident microwave radiation is at resonance with the magnetic field-dependent Zeeman energy, meaning the photon energy of the incident radiation matches the energy-level separation of unpaired electrons in an applied static field, $B_0$. The energy level scheme of Zeeman splitting for a $S = \frac{1}{2}$ system is plotted out in figure 2.1. [9]

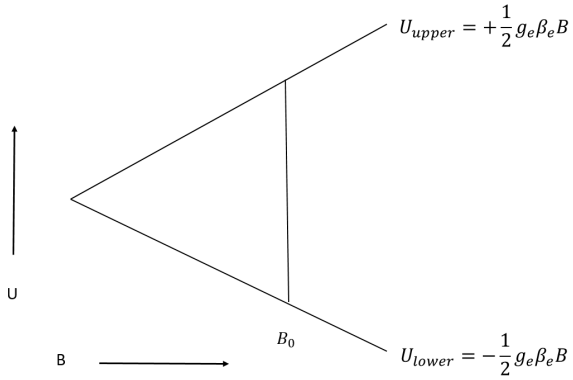


Figure 2.1: Field-dependent Zeeman splitting for a $S = \frac{1}{2}$ system

## 2.2 Hyperfine Interaction

In addition to the interaction with an applied static magnetic field, the presence of nuclear magnetic dipoles in the sample also contributes to the structure of electron spin states. The doublet line structure for a $S = \frac{1}{2}$ system will further split into $(2S+1)(2I+1)$ energy states through a nuclear hyperfine interaction between an unpaired electron and a nearby nucleus. The hyperfine interaction is made up of a through-space dipolar distribution and a direct Fermi contact contribution. The energy of the electron-nuclear dipole interaction is expressed as

$$U_{dipolar} = -\frac{\mu_0}{4\pi} \frac{3\cos^2\theta - 1}{r^3} \mu_{nz} \mu_{ez} = -B_{local} \mu_{ez}$$

The local field $B_{local}$ induced by the nucleus at the electron vanishes when the interaction energy $U_{dipolar}$ is averaged over the electron probability distribution function in an isotropic system such as a liquid, where the electron is not localized in space. Considering equal probability for all $\theta$ values,

$$< \cos^2\theta >= \frac{\int_0^{2\pi} \int_0^{\pi} \cos^2\theta \sin\theta d\theta d\varphi}{\int_0^{2\pi} \int_0^{\pi} \sin\theta d\theta d\varphi} = \frac{1}{3}$$

The element $\sin\theta d\theta d\varphi$ is the infinitesimal surface area on a sphere in spherical coordinates. As $3 < \cos^2\theta >= 1$, this through-space dipolar interaction is averaged out. [9]

The isotropic hyperfine interaction is predominantly given by a Fermi contact term, with energy

$$U_{iso} = -\frac{2\mu_0}{3}|\psi(0)|^2\mu_{ez}\mu_{nz}$$

Here $\psi(0)$ represents the electron wavefunction amplitude at the nucleus. Only electrons in s orbitals have a non-zero probability density at the nucleus and give rise to an isotropic hyperfine interaction. This hyperfine interaction is isotropic due to the spherical symmetry of s orbitals. [9]

The energy spectrum of a quantum-mechanical system is determined by solving the time-independent Schrödinger equation:

$$\mathcal{H}\phi_k = U\phi_k$$

Here the Hamiltonian operator $\mathcal{H}$ is the operator for the total energy, the index $k$ is labeling the eigenstates of the system, and $\phi_k$ is the eigenfunction of the $z$ component of the spin angular momentum as well as the energy. The Hamiltonian is represented by a matrix generated from angular-momentum basis operators in quantum-mechanical state space. Combining electronic and nuclear Zeeman interactions with the hyperfine interaction yields a spin Hamiltonian consisting spin operators with varying relative strengths

$$\mathcal{H} = g\beta_e BS_Z - g_n\beta_n BI_Z + A_0 I_Z S_Z$$

$$A_0 = \frac{2\mu_0}{3}g\beta_e\beta_n|\phi(0)|^2$$

Here $A_0$ is the isotropic hyperfine coupling constant that measures the magnetic interaction energy between the electron and the nucleus. An example of energy levels computed using the spin-Hamiltonian operator $\mathcal{H}$ with electron spin $S = \frac{1}{2}$ and nuclear spin $I = 1$ is

$$\begin{aligned}
U_{+\frac{1}{2},+1} &= \frac{1}{2}g\beta_e B - g_n\beta_n B + \frac{1}{2}A_0 & \qquad U_{-\frac{1}{2},-1} &= -\frac{1}{2}g\beta_e B + g_n\beta_n B + \frac{1}{2}A_0 \\
U_{+\frac{1}{2},0} &= \frac{1}{2}g\beta_e B & \qquad U_{-\frac{1}{2},0} &= -\frac{1}{2}g\beta_e B \\
U_{+\frac{1}{2},-1} &= \frac{1}{2}g\beta_e B + g_n\beta_n B - \frac{1}{2}A_0 & \qquad U_{-\frac{1}{2},+1} &= -\frac{1}{2}g\beta_e B - g_n\beta_n B - \frac{1}{2}A_0
\end{aligned}$$

The energy level scheme of hyperfine splitting for a $S = \frac{1}{2}, I = 1$ system as well as the CW ESR spectrum of a representative nitroxide radical (TEMPO) in solution are plotted out in figure 2.2. [9]

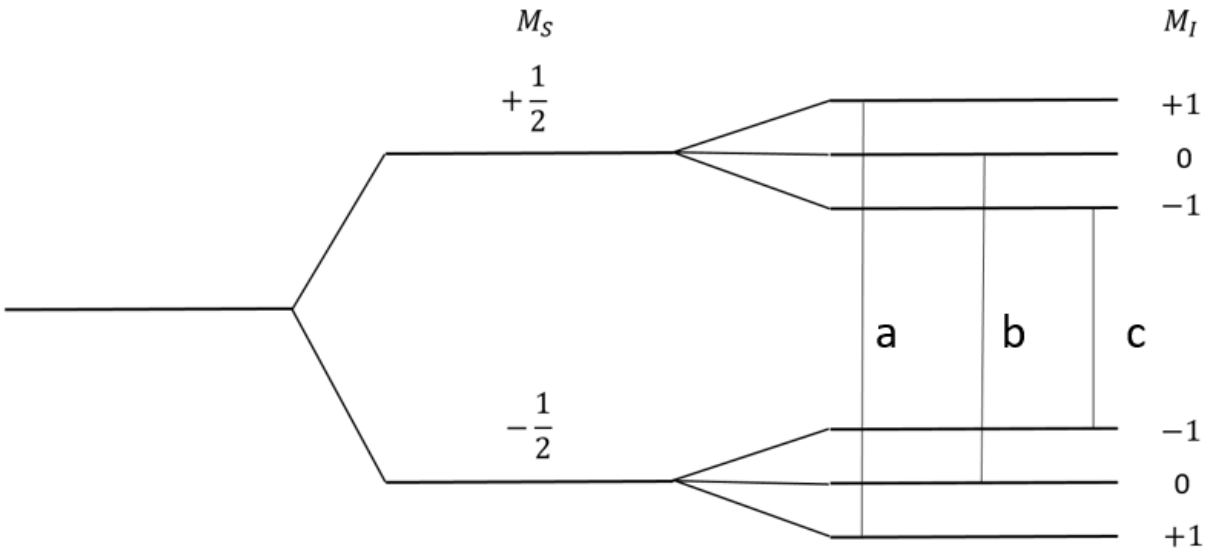


(a)

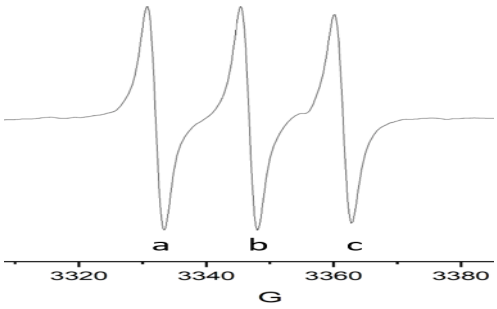


(b)

Figure 2.2: (a) Energy level schematic for an isotropic hyperfine-coupled S=1/2, I=1 spin system. (b) x-band CW ESR spectrum of TEMPO in chloroform solution: the resonance lines correspond to the transitions between energy levels with the same label.

## 2.3 Electron Zeeman g- Anisotropy

Zeeman and hyperfine interactions are generally anisotropic and orientation dependent. For a magnetically isotropic system such as a dilute liquid solution of low viscosity, the Zeeman splitting and hyperfine splitting are independent of orientations as discussed in previous sections. A measured ESR spectrum of a liquid system is time-averaged over all orientations as a result of rapid, random reorientation of solute molecules, while a ESR spectrum of oriented species in a solid is dependent on the molecular orientation of the paramagnetic species relative to the quantizing static magnetic field direction. The $g$ factor and the hyperfine coupling are represented as tensors that are diagonal in their principal axis system. The anisotropy of the $g$ factor specifically arises from the coupling between the electron spin and the electronic orbital angular momentum. The $g$ factor is defined as

$$g = [n^T \cdot (g \cdot g^T) \cdot n]^{\frac{1}{2}}$$

Here $\vec{n}$ is a unit vector along $\vec{B}$ which is a function of relative sample orientation to $\vec{B}$.

$$\vec{n} = \frac{\vec{B}}{B} = \begin{vmatrix} c_x \\ c_y \\ c_z \end{vmatrix}$$

Since $gg \equiv g \cdot g^T$ and $(gg)_{ij} = (gg)_{ji}$,

$$g^2 = \begin{vmatrix} c_x & c_y & c_z \end{vmatrix} \cdot \begin{vmatrix} (gg)_{xx} & (gg)_{xy} & (gg)_{xz} \\ (gg)_{yx} & (gg)_{yy} & (gg)_{yz} \\ (gg)_{zx} & (gg)_{zy} & (gg)_{zz} \end{vmatrix} \cdot \begin{vmatrix} c_x \\ c_y \\ c_z \end{vmatrix}$$

where $(gg)_{ij}$ means a $gg$ component along the $i$ axis when the magnetic field is applied along $j$, and this component can be determined experimentally by rotating the sample with the magnetic field fixed in the $xz$, $yz$, and $xy$ planes. For the $xz$ plane with $\varphi = 0$, $\theta$ is the angle between $B$ and $z$ axis as plotted in figure 2.3. [9]

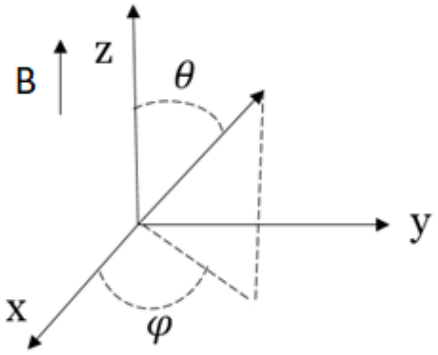


Figure 2.3: Laboratory frame in spherical coordinate system.

Then

$$g^2 = \begin{vmatrix}\sin\theta & 0 & \cos\theta\end{vmatrix} \cdot \begin{vmatrix}(gg)_{xx} & (gg)_{xy} & (gg)_{xz} \\ (gg)_{yx} & (gg)_{yy} & (gg)_{yz} \\ (gg)_{zx} & (gg)_{zy} & (gg)_{zz}\end{vmatrix} \cdot \begin{vmatrix}\sin\theta \\ 0 \\ \cos\theta\end{vmatrix}$$

and

$$g^2 = (gg)_{xx}\sin^2\theta + 2(gg)_{xz}\sin\theta\cos\theta + (gg)_{zz}\cos^2\theta$$

Similarly, for rotation in the $yz$ plane with $\varphi = 90°$

$$g^2 = (gg)_{yy}\sin^2\theta + 2(gg)_{yz}\sin\theta\cos\theta + (gg)_{zz}\cos^2\theta$$

Likewise, for rotation in the $xy$ plane with $\theta = 90°$

$$g^2 = (gg)_{xx}\cos^2\varphi + 2(gg)_{xy}\sin\varphi\cos\varphi + (gg)_{yy}\sin^2\varphi$$

The $gg$ matrix may be transformed to a diagonal form by finding a matrix $C$ that can perform rotation of the principal axes $X$, $Y$, $Z$ of the $g$ tensor to align with the laboratory axes $x$, $y$, $z$

$$C = \begin{vmatrix}C_{Xx} & C_{Xy} & C_{Xz} \\ C_{Yx} & C_{Yy} & C_{Yz} \\ C_{Zx} & C_{Zy} & C_{Zz}\end{vmatrix}$$

such that

$$C \cdot \begin{vmatrix} (gg)_{xx} & (gg)_{xy} & (gg)_{xz} \\ (gg)_{yx} & (gg)_{yy} & (gg)_{yz} \\ (gg)_{zx} & (gg)_{zy} & (gg)_{zz} \end{vmatrix} \cdot C^T = \begin{vmatrix} (gg)_{xx} & 0 & 0 \\ 0 & (gg)_{yy} & 0 \\ 0 & 0 & (gg)_{zz} \end{vmatrix}$$

Hence

$$g_{PAS} = \begin{vmatrix} (gg)_{xx} & 0 & 0 \\ 0 & (gg)_{yy} & 0 \\ 0 & 0 & (gg)_{zz} \end{vmatrix}$$

A simulated ESR spectrum with respect to $g$-anisotropy can be derived from the eigenvalues of the spin Hamiltonian, which is a Lorentzian line centered at $\omega$ with amplitude given by diagonalizing $\mathcal{H}(\theta, \varphi)$. By transforming the principal axis system of the $g$ factor to the laboratory frame defined by the $z$-axis of the applied magnetic field, the effective $g$ factor is

$$g(\theta, \varphi) = R(\theta, \varphi) \cdot g_{PAS} \cdot R(\theta, \varphi)^{\dagger}$$

Here $\theta$, $\varphi$ are spherical spatial coordinates of the molecular principal axis frame relative to the laboratory frame, assuming the tensor frame, the molecular frame, and the crystal frame $z$-axes coincide.

The orientation-dependent Hamiltonian describing the Zeeman splitting is

$$\mathcal{H} = \beta S \cdot g \cdot B$$

The corresponding resonant frequency is calculated from the eigenvalues of the Hamiltonian, and the single-orientation spin spectrum is given by a Lorentzian lineshape function derived from solving the Bloch equations centered at the resonant frequency. The ESR spectrum of a sample containing multiple orientations is generated by averaging signals of all orientations over a sphere, weighted by a probability distribution of orientations.

$$S(\omega) = \int s(\theta, \varphi, \omega) P(\theta, \varphi) \sin\theta d\theta d\varphi$$

$S(\omega)$ is the simulated ESR spectrum, $s(\theta, \varphi, \omega)$ is the ESR signal at a given orientation, and $P(\theta, \varphi)$ is the probability distribution of orientations which contains information about the sample structure.

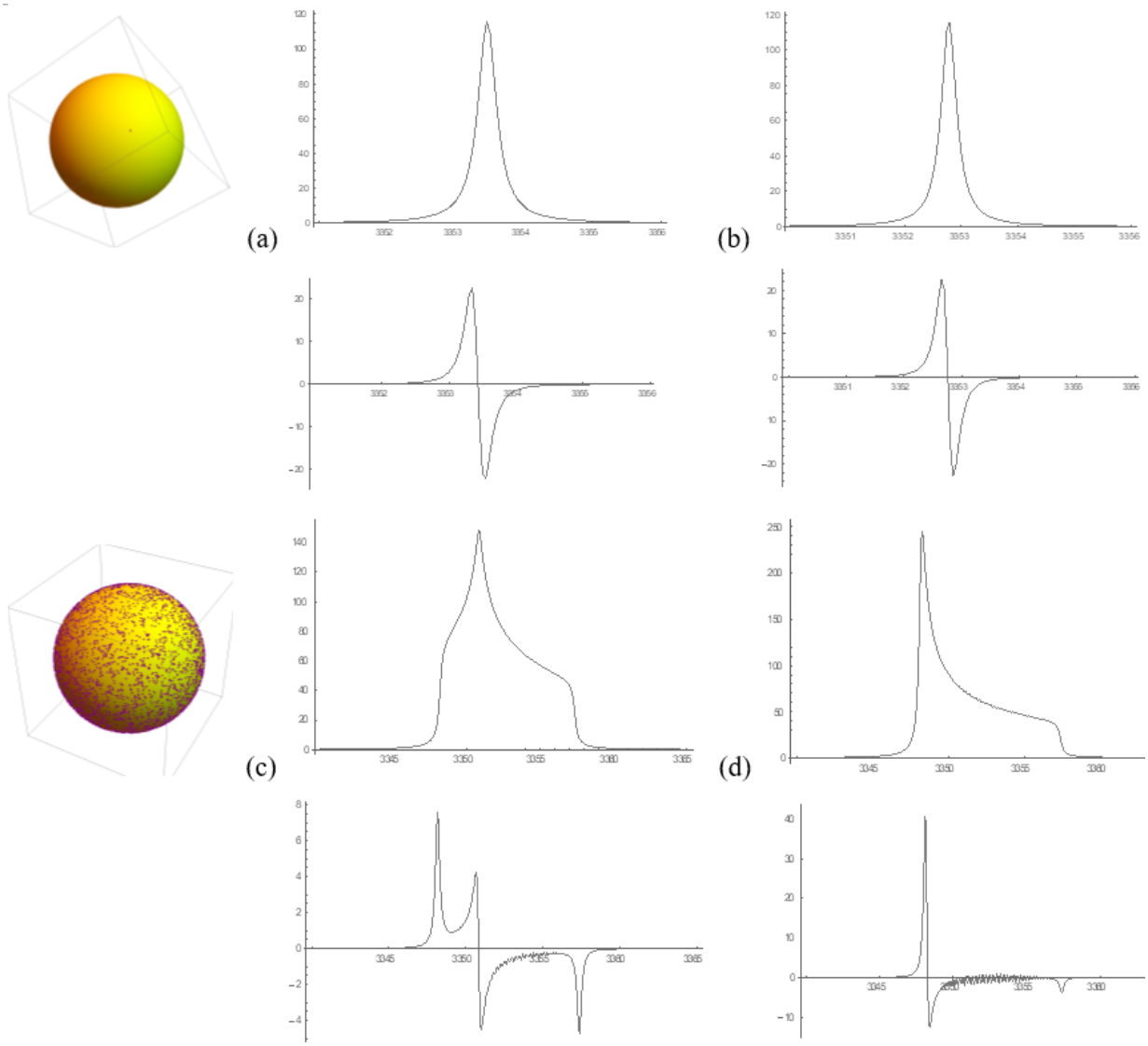


Figure 2.4: Simulated ESR absorption spectra and first derivative (under absorption) with a $g$ tensor ($g_{xx}$=2.0029, $g_{yy}$=2.0013, $g_{zz}$=1.9974): (a) cubic crystal [111]; (c) powder (3D); with a $g$ tensor for molecules possessing axial symmetry ($g_{xx}$=$g_{yy}$=2.0029, $g_{zz}$=1.9974): (b) cubic crystal [111]; (d) powder (3D). The illustration of sample points are shown on the left.

Several simulations of ESR absorbance and corresponding first derivative spectrum are shown in figure 2.4 for two solid-state systems with different g tensors and varying amount

of molecular ordering. The spectra show a single peak for a cubic crystal, while the spectra for a powder sample are space-averaged over all orientations with equal probability. The center field and lineshape of a crystalline sample are dependent on orientation in the magnetic field, and is shown in figure 2.5 by placing a single-electron perchloro triphenyl methyl (PTM) radical crystal sample with minimal hyperfine interactions in an ESR sample tube and rotating the tube to measure with different relative angles to the magnetic field. This spectrum of PTM is explained with simulations in the appendix.

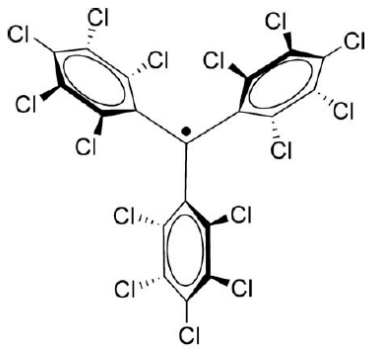


(a)

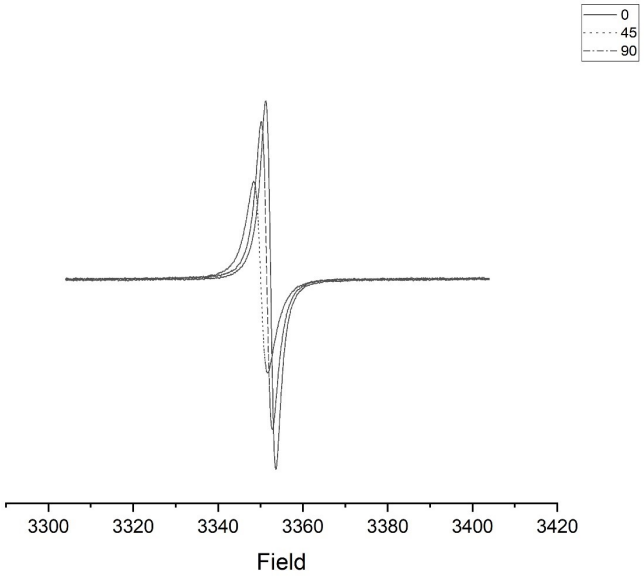


(b)

Figure 2.5: (a) Structure of PTM molecule [10]; (b) Orientation dependence of PTM crystal sample ($10^{14}$ spins).

## 2.4 Hyperfine Anisotropy

The anisotropic part of the hyperfine coupling originates from the through-space dipolar interaction between an electron and a nucleus. This term is non-zero for solid-state systems, while in a liquid system of low viscosity, this dipole-dipole interaction is time-averaged to zero. The interaction energy between an electron dipole and a nuclear dipole separated by a distance $r$, as shown in figure 2.6, is

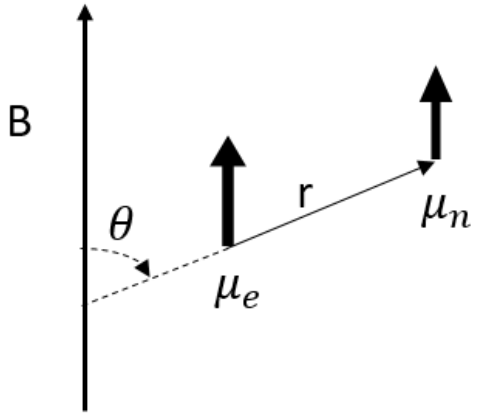


Figure 2.6: Interaction of an aligned electronic spin dipole $\mu_e$ and a nearby nuclear spin dipole $\mu_n$.

$$U_{dipolar}(\vec{r}) = \frac{\mu_0}{4\pi}[\frac{\vec{\mu_e}^T \cdot \vec{\mu_n}}{r^3} - \frac{3(\vec{\mu_e}^T \cdot \vec{r})(\vec{\mu_n}^T \cdot \vec{r})}{r^5}]$$

The Hamiltonian, neglecting the g anisotropy in the magnetic moment, is

$$\mathcal{H}_{dipolar}(\vec{r}) = -\frac{\mu_0}{4\pi} g\beta_e g_n \beta_n [\frac{S \cdot I}{r^3} - \frac{3(S \cdot r)(I \cdot r)}{r^5}]$$

The Hamiltonian form is calculated using the average over the electron spatial distribution.

$$\mathcal{H}_{dipolar}(\vec{r}) = -\frac{\mu_0}{4\pi} g\beta_e g_n \beta_n \times \begin{vmatrix} S_x & S_y & S_z \end{vmatrix} \cdot \begin{vmatrix} < \frac{r^2-3x^2}{r^5} > & < -\frac{3xy}{r^5} > & < -\frac{3xz}{r^5} > \\ < -\frac{3yx}{r^5} > & < \frac{r^2-3y^2}{r^5} > & < -\frac{3yz}{r^5} > \\ < -\frac{3zx}{r^5} > & < -\frac{3zy}{r^5} > & < \frac{r^2-3z^2}{r^5} > \end{vmatrix} \cdot \begin{vmatrix} I_x \\ I_y \\ I_z \end{vmatrix} = S \cdot T \cdot I$$

The full spin Hamiltonian includes both the isotropic and anisotropic hyperfine terms, as well as the electron and nuclear Zeeman terms:

$$\mathcal{H} = \beta_e S \cdot g \cdot B + S \cdot A \cdot I - \beta_n I \cdot g_n \cdot B$$

$$A = A_0 1_3 + T$$

Here $A_0$ is the isotropic hyperfine contact interaction, and $1_3$ is a $3 \times 3$ unit matrix. [9]

## 2.5 Spin Hamiltonian for Two Interacting Electrons

In addition to the Zeeman and hyperfine contributions to the spin Hamiltonian discussed above for one unpaired electron, the electron-exchange interaction and electron-electron dipole interaction also become important when the electron spin concentration is high.

The Heisenberg exchange interaction is usually isotropic and leads to homogeneous line broadening, represented by the spin Hamiltonian

$$(\mathcal{H}_{exch})_{iso} = S_1 \cdot J_0 \cdot S_2$$
$$J_0 = -2 < \psi_a(1)\psi_b(2)|\frac{e^2}{4\pi\varepsilon_0 r}|\psi_a(2)\psi_b(1) >$$

Here $S_1$ and $S_2$ are the electron-spin operators, $J_0$ is the isotropic electron-exchange coupling constant not taking account of the coulombic interaction between the electrons, $\psi_a$ and $\psi_b$ are different normalized spatial molecular-orbital wavefunctions, $\varepsilon_0$ is the vacuum permittivity, and $r$ is the inter-electron distance. The line width broadening is related to the exchange frequency, and multiple lines may collapse into a single exchange-narrowed line under strong exchange. The averaging of the hyperfine interaction due to strong exchange is shown in figure 2.7. [9]

The dipole-dipole coupling for two interacting unpaired electrons is analogous to the anisotropic hyperfine interaction and leads to homogeneous broadening of each line. The electron dipole-dipole spin-Hamiltonian can be expressed through a tensor, $D$, as

$$\mathcal{H}_{SS} = S_1 \cdot D \cdot S_2$$
$$S = S_1 + S_2$$

$D$ is averaged over the electronic spatial wavefunction and can also be diagonalized. The electron spin-orbit coupling and the generalized anisotropic exchange interaction lead to the same spin-Hamiltonian term. The effective spin Hamiltonian for two interacting electrons is obtained as

$$\mathcal{H} = \beta S \cdot g \cdot B + S \cdot D \cdot S + \frac{1}{2}J_0[S^2 - \frac{3}{2}1]$$

where the last term is given by the vector cosine sum rule. [9]

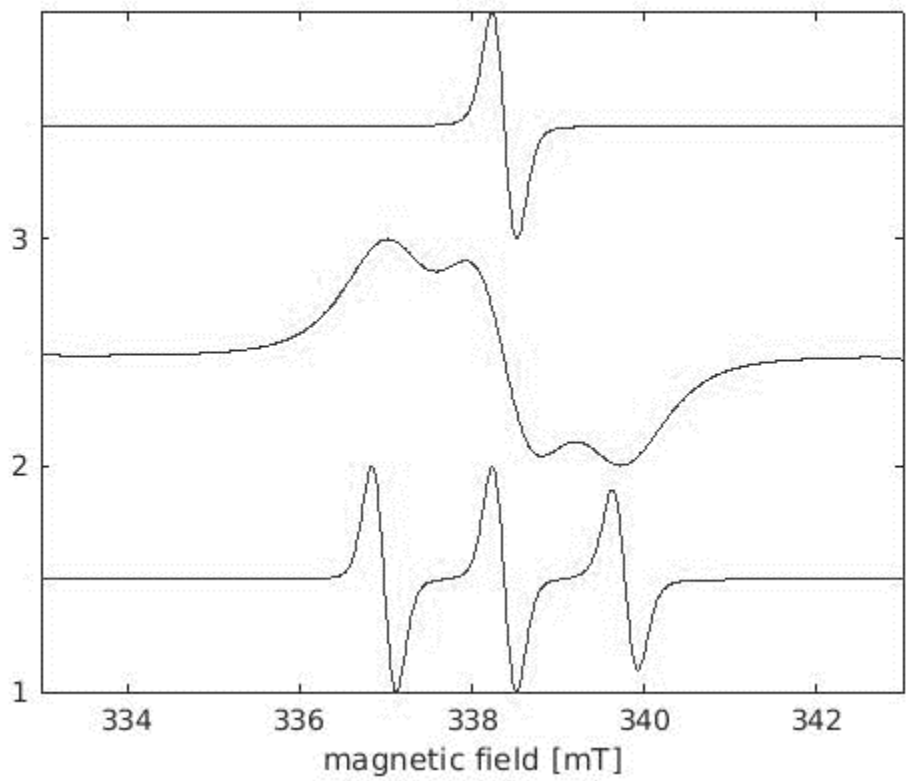


Figure 2.7: Simulation of nitroxide spectrum with increasing exchange frequency from 1 to 3 referring to 1, 100, 1000MHz (1mT=10G).

## 2.6 Spin Relaxation and Bloch Equations

The time dependence of the total spin magnetization vector $M$ in applied external static and oscillating magnetic fields can be described using the Bloch equations [9]. In the frame rotating about the $z$ direction at the angular frequency $\omega$, the Bloch equations with the static magnetic field $B$ taken along $z$ and a monochromatic oscillating field $B_1$ sinusoidally varying at $\omega$ perpendicular to $B$ ($B_{1x} = B_1 \cos \omega t, B_{1y} = B_1 \sin \omega t, B_{1z} = 0$) are

$$\frac{dM_x}{dt} = -(\omega_B - \omega)M_y - \frac{M_x}{T_2}$$

$$\frac{dM_y}{dt} = (\omega_B - \omega)M_x + \gamma_e B_1 M_z - \frac{M_y}{T_2}$$

$$\frac{dM_z}{dt} = -\gamma_e B_1 M_y - \frac{M_z - M_z^0}{T_1}$$

where $\omega_B = -\gamma_e B$ is the Larmor frequency, $T_2$ is the transverse relaxation time assuming the transverse components $M_x$ and $M_y$ relax at the same rate, $T_1$ is the spin-lattice relaxation time, and $M_z^0$ is the equilibrium value of $M_z$. The steady-state solutions of the Bloch equations are

$$\frac{dM_x}{dt} = -M_z^0 \frac{\gamma_e B_1 (\omega_B - \omega) T_2^2}{1 + (\omega_B - \omega)^2 T_2^2 + \gamma_e^2 B_1^2 T_1 T_2}$$

$$\frac{dM_y}{dt} = +M_z^0 \frac{\gamma_e B_1 T_2}{1 + (\omega_B - \omega)^2 T_2^2 + \gamma_e^2 B_1^2 T_1 T_2}$$

$$\frac{dM_z}{dt} = +M_z^0 \frac{1 + (\omega_B - \omega)^2 T_2^2}{1 + (\omega_B - \omega)^2 T_2^2 + \gamma_e^2 B_1^2 T_1 T_2}$$

In an experimental setup, the $B_1$ field usually oscillates linearly in the (say) x direction ($B_{1x} = 2B_1 \cos \omega t, B_{1y} = 0, B_{1z} = 0$), and it can be decomposed into two oppositely rotating fields with equal-magnitude, whose effects are described by the dynamic susceptibilities. For electrons,

$$M = \chi H = \chi B / \kappa \mu_0$$

where $\mu_o$ is the vacuum permeability, and $\kappa$ is the relative parameter describing the medium. The sample equilibrium macroscopic magnetization is then

$$M_z^0 = \chi^0 B / \kappa \mu_0 = \frac{1}{2} g \beta_e \Delta N^{ss} / V$$

where $\chi^0 = \kappa \mu_0 N_V g^2 \beta_e^2 / 4 k_B T$ is the static magnetic susceptibility with the spin volume density $N_V$, and $\Delta N^{ss}$ is the steady state population difference for electrons in a volume $V$. The dynamic susceptibilities $\chi'$ and $\chi$" are defined to represent the emission and power absorption:

$$\chi' = +\kappa \mu_0 M_x / B_1$$

$$\chi'' = -\kappa \mu_0 M_y / B_1$$

The power absorbed by the magnetic system from the linearly polarized excitation field is

$$P_a(\omega) = 1\frac{\omega\chi'' B_1^2}{\mu_0 V} = \frac{\pi}{\mu_0}\frac{B_1^2}{(1+\gamma_e^2 B_1^2 T_1 T_2)^{\frac{1}{2}}}\omega\omega_B\chi^0 Y$$

where $Y(\omega - \omega_B)$ is a normalized Lorentzian function with half width at half-height (FWHM) given by $\frac{1}{|\gamma_e| T_2}(1+\gamma_e^2 B_1^2 T_1 T_2)^{\frac{1}{2}}$.

To avoid power broadening in CW ESR measurements, the saturation term, $\gamma_e^2 B_1^2 T_1 T_2$, must be kept small. This is normally accomplished in practice by adjusting an attenuator to limit $B_1$ for given $T_1$ and $T_2$ relaxation times.

# Chapter 3

# Fabrication of Langmuir-Blodgett Films

Monolayer LB film samples were prepared on a vibration-isolated KSV NIMA Langmuir-Blodgett deposition trough contained in a laminar flow hood. The LB trough used for this work is 50mm wide with an area of 7500mm$^2$. Stock spin-labeled amphiphiles and chloroform solution were purchased from SIGMA ALDRICH, and the quartz substrate wafer used for fabrication was purchased from UNIVERSITY WAFER (Single Crystal Quartz 2298). The wafer was cut into pieces with appropriate size for mounting in the ESR sample tubes using a DISCO Automatic dicing saw (DAD3240), shown in figure 3.2.

## 3.1 Materials

Stearic acid and its oxazolidine derivative, 16-doxyl-stearic acid (16-DSA), shown in figure 3.1, were used directly from a stock solution kept in a refrigerator at 4°C. This oxazolidine derivative contains a nitroxide radical moiety that can be detected by ESR spectroscopy.

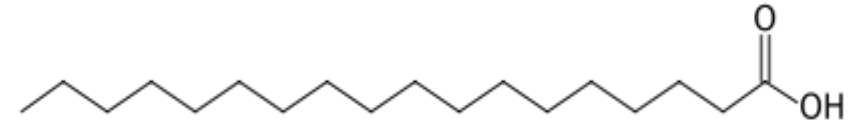


(a)

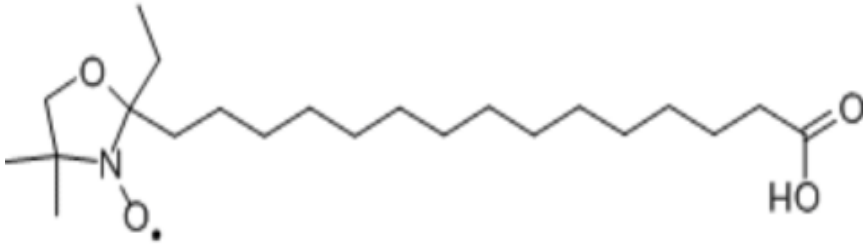


(b)

Figure 3.1: Molecular structure of (a) stearic acid [29]; (b) 16-DSA [28].

Chloroform with purity higher than 99.8% was used to prepare a spreading solution of 16-DSA or 16-DSA and stearic acid mixture with a concentration of $1.3 \times 10^{-3}$mol/L.

The subphase used for LB preparation was Millipore-Q grade water with pH 5.3.

## 3.2 Substrate Dicing

The substrates used for LB film deposition were diced from a 0.5mm thick double-side polished single crystal quartz wafer. Before the dicing process, a UV film is applied to the wafer and wafer frame by a Ultron wafer/frame film applicator. Then, the wafer assembly is loaded on to a dicing saw and automatically cut in vacuum with input size 4mm×30mm. The resulting size of the substrate was 3.78×30mm due to the width of the dicing blade (0.22mm). After dicing, the assembly was dried with an air gun to remove excess water and transferred to a Ultron UV curing system for finishing.

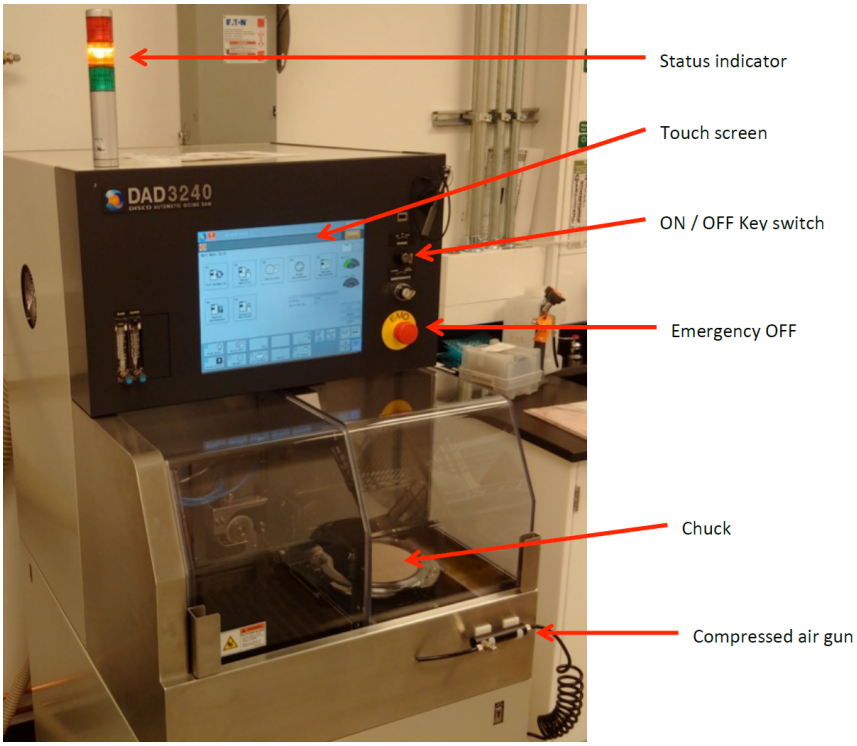


Figure 3.2: DISCO dicing saw located at Quantum-Nano Fabrication and Characterization Facility (QNFCF).

## 3.3 Creation of a Langmuir Film

The Langmuir-Blodgett trough consists of a shallow trough with hydrophobic edges as well as hydrophobic poly(tetrafluoroethylene) (PTFE) barriers as shown in figure 3.3 [5]. An electronic interface connected to a computer monitors surface pressure, and the entire experiment is controlled and monitored by software provided by KSV NIMA [17].

For creation of LB films, the trough is first slightly overfilled with water and aspirated to thoroughly clean the subphase surface. Then, spin samples dissolved in a volatile non-polar solvent are spread on the water surface with a microliter syringe. Chloroform is used as the volatile solvent in this experiment, but hexane or benzene are also commonly used [5]. The solution spreads rapidly on the surface, and a monolayer forms after the volatile solvent evaporates.

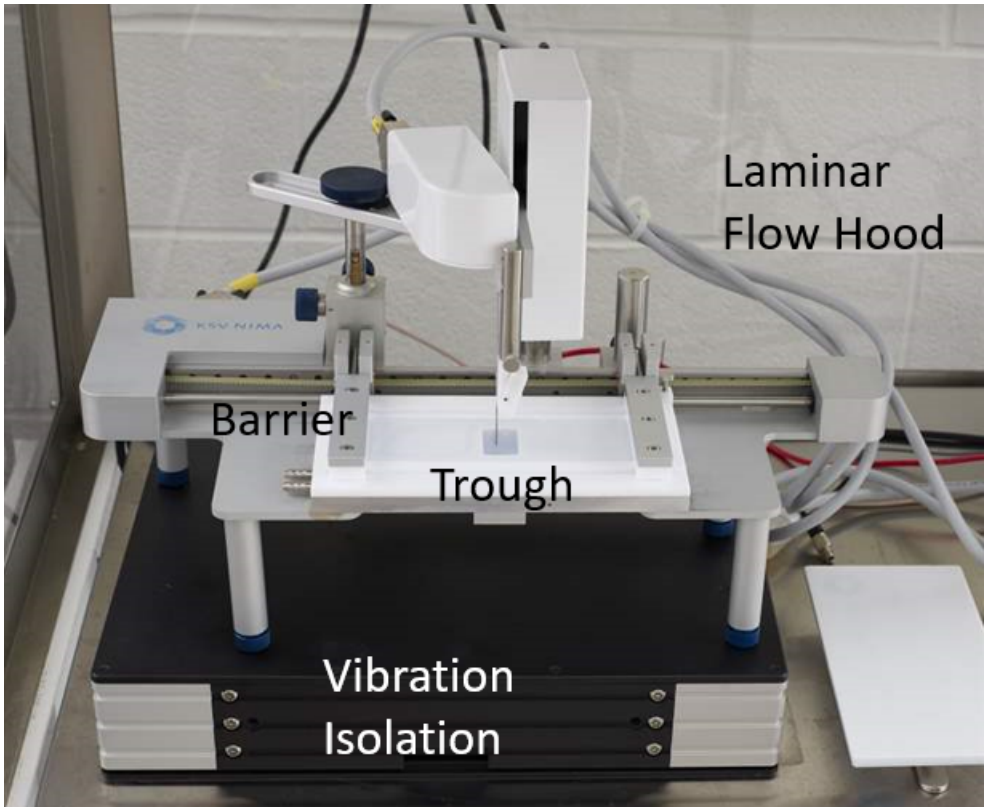


Figure 3.3: KSV NIMA Langmuir-Blodgett trough [34].

## 3.4 Spreading Isotherm

LB monolayers can be compressed or expanded by sliding the barriers along the edges of the trough, and a spreading isotherm of surface pressure versus mean molecular area is recorded by compressing the film at a constant rate and at constant temperature. The measurement of surface tension by a balance with a polished Wilhelmy rod indicates surface free energy. Surface pressure is given by the decrease in surface tension

$$\Pi = \gamma - \gamma_0$$

where $\gamma$ is the surface tension in the absence of a monolayer, and $\gamma_0$ is the surface tension with the monolayer present [17]. The high surface tension of water is easily reduced by contaminants. Thus, it is critical to ensure cleanliness and prevent contamination in the

process. The trough system, including trough, barriers, sample clamp, and aspirator tip, is rinsed with pure ethanol and millipore water, then wiped with a KimWipe tissue. The tweezer, spatula, and beakers are rinsed with acetone and ethanol, then wiped with a KimWipe tissue. The Wilhelmy rod is rinsed with ethanol and water. The substrates are sonicated in toluene, acetone, ethanol, and millipore water bath in order for 10 minutes each. The cleanliness of the subphase is ensured by aspirating the surface while compressing the barriers, and this procedure is repeated until the surface pressure stays below 0.2-0.3 mN/m during the compression; then the subphase surface may be considered clean [16].

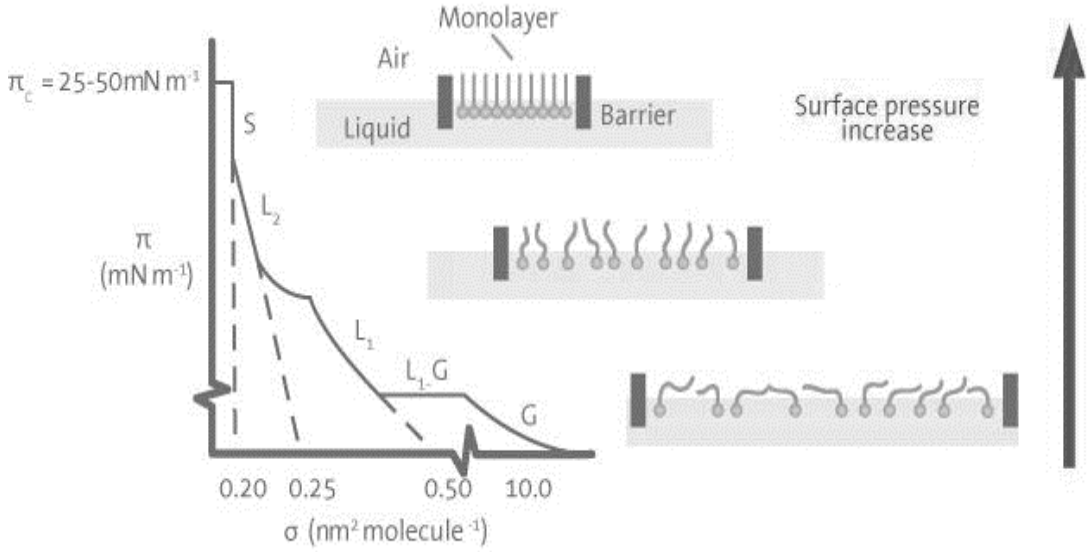


Figure 3.4: Schematic isotherm of subphase surface pressure versus mean molecular area (left) and orientation of the surfactants in different phases: the molecules are squeezed together as the barriers are compressed[17].

In figure 3.4, it is possible to recognize four distinct phases by examining the slope of the isotherm. When the area between the barriers is large, adjacent molecules are far from each other, so the monolayer can be considered as a two-dimensional gas (G) with weak interactions between molecules. As the barriers close, the film undergoes a phase transition to a liquid-expanded state ($L_1$). Upon further compression, the $L_1$ phase transits to a liquid-condensed state ($L_2$), and finally reaches a solid state (S). If compressed further after achieving the solid state, the monolayer will collapse, leading to a rapid drop of surface pressure. A given monolayer may not exhibit all the discussed features because of the fairly narrow range of temperatures and surface pressures available in practice. [17]

The spreading isotherm of 16-DSA on pure water subphase with pH 5.3 is recorded at room temperature (296K) and provides useful information about the sample. The pH value and temperature are measured by probes mounted on the LB trough.

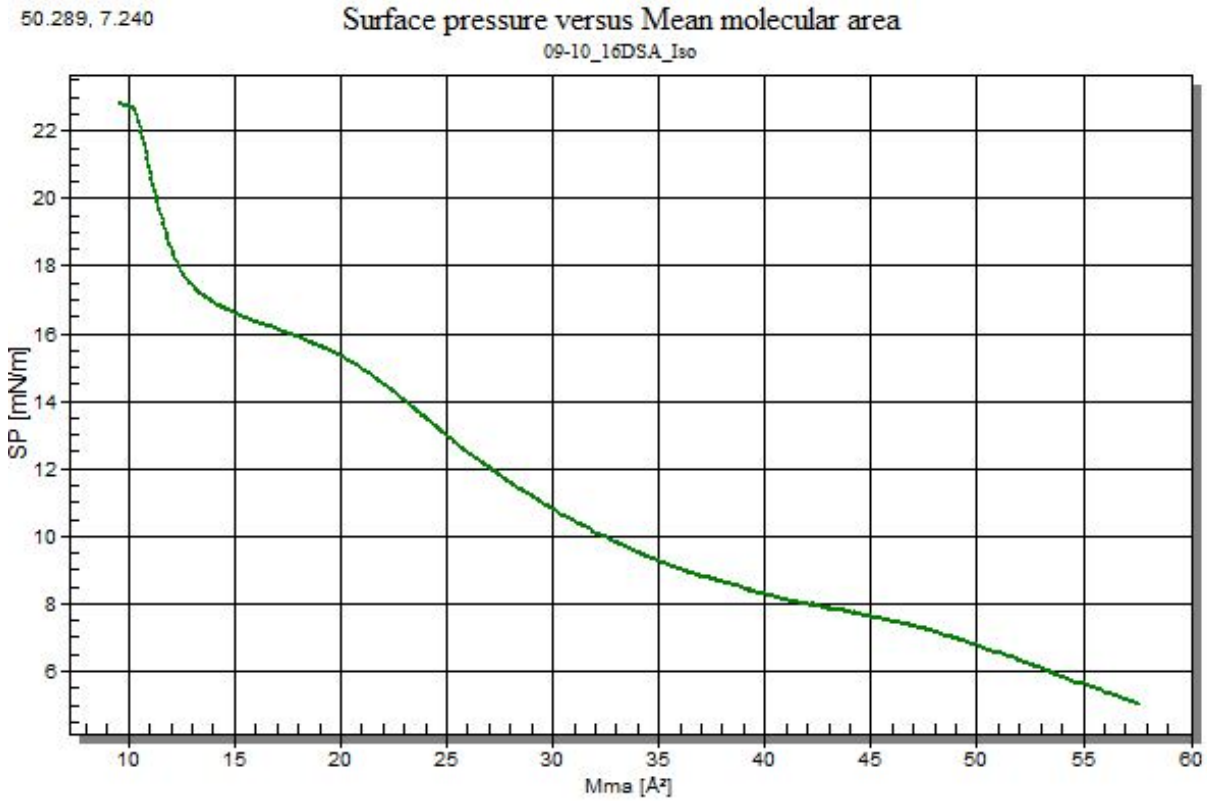


Figure 3.5: Experimental isotherm of 16-DSA on pure water.

In figure 3.5, the isotherm of 16-DSA is recorded with a concentration low enough such that the molecules are initially taken to be non-interacting. As intermolecular distances decrease, the surface pressure rises gradually until collision happens at a mean molecular area less than 10 $Å^2$/molecule at a surface pressure of around 22.1 mN/m, which are consistent with literature [4]. The characteristic plateau region occurring at a surface pressure around 15-16 mN/m indicates a transition from a close-packed bent structure to an upright conformation with a strong reduction of the limiting area[4, 31].

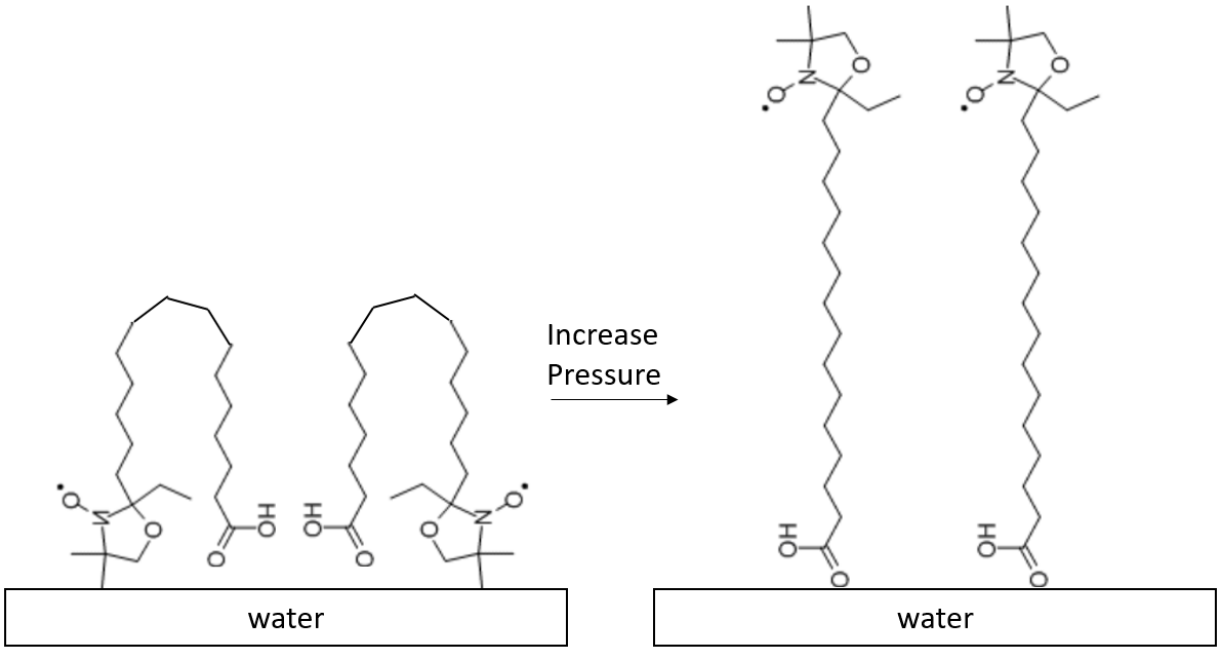


Figure 3.6: Schematic illustration for orientation of 16-DSA molecules on a water subphase for different surface pressures.

As shown in figure 3.6, the 16-DSA molecules are bent over on water subphase at low surface pressure because of the affinity of the doxyl group to water, and correspondingly, the molecules occupy a larger area than the upright standing structure. When the surface pressure increases, the long hydrophobic tails are forced to align, and smaller areas are taken by the molecules with the tails normal to the water surface. This feature is more pronounced for 16-DSA than other types of doxyl stearic acid since the doxyl group is located closer to the acid head group in other types[4].

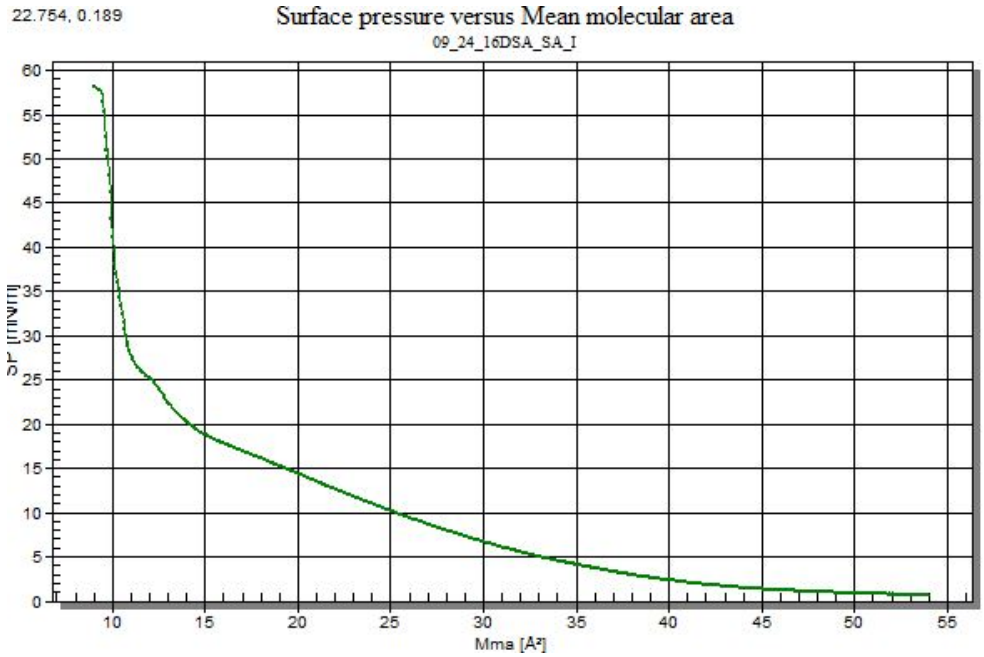


Figure 3.7: Experimental isotherm of 16-DSA and stearic acid mixture on pure water.

An isotherm of diluted 16-DSA sample which is prepared by mixing 16-DSA molecules with stearic acid molecules in a 1:2 ratio is also measured, shown in figure 3.7. The signature plateau region is now reduced and appears at a higher surface pressure around 25 mN/m.

## 3.5 Film Deposition on a Solid Substrate

Solid-supported LB films are formed by dipping a solid substrate through the floating monolayer while the surface pressure is kept constant, allowing amphiphiles to be physisorbed onto the substrate. For sufficient adhesion of the monolayer to the substrate, the surface pressure should be high enough so that the monolayer does not fall apart during the transport to the substrate, but it should not be too high that the monolayer collapses during deposition. Thus, deposition is normally carried out with the monolayer in a condensed state with a surface pressure ranging from 20 to 40 mN/m[5]. The quality of deposition is measured by the transfer ratio and is equal to 1 for ideal transfer [17]. If transfer ratio is larger than 1, it indicates instability in the film or multilayer is transferred.

$$\text{Transfer ratio} = \frac{\text{trough area reduced by barriers}}{\text{substrate area deposited}}$$

$$\text{Transfer} = \frac{\text{total trough area reduced by barriers}}{\text{total substrate area}}$$

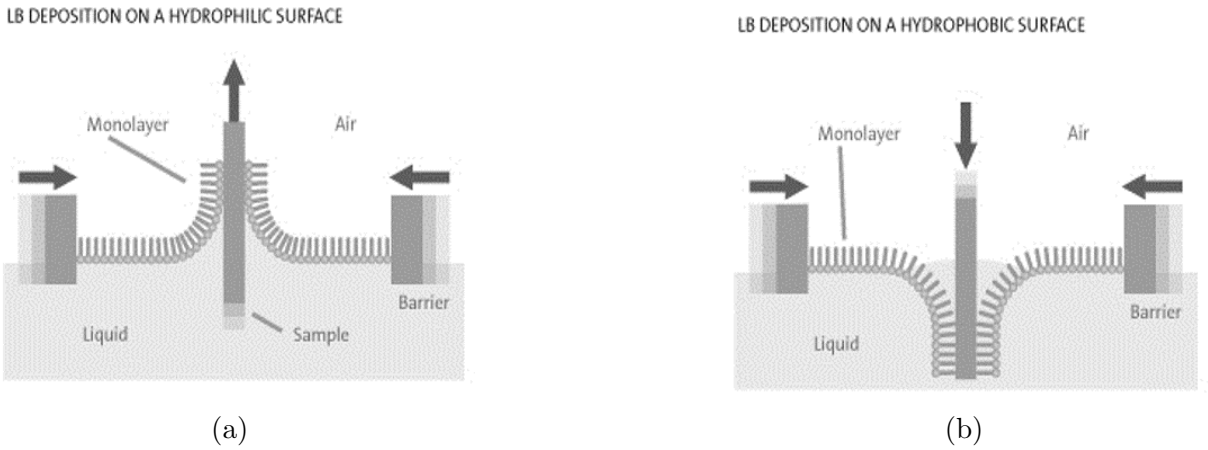


(a) (b)

Figure 3.8: Different types of deposition of floating monolayers onto a solid substrate: (a) monolayer on a hydrophilic substrate; (b) monolayer on a hydrophobic substrate[17].

The direction of deposition depends on the nature of the substrate: As shown in figure 3.8, for the first layer, a hydrophilic substrate is raised from the subphase through the monolayer, whereas a hydrophobic substrate is lowered into the subphase through the monolayer. Common choices of solid substrates are glass, mica, silicon, and quartz, depending on the desired use [5]. Single crystal quartz was chosen for our ESR application due to its desirable microwave dielectric properties (low tangent loss and high susceptibility).

The previously diced quartz substrates were cleaned and stored in water ahead of the deposition. Then, the chloroform solution of 16-DSA was spread on the subphase surface. After waiting at least 10 minutes for the chloroform to evaporate, the isotherm is recorded with a compression rate of 5mm/min. Once the target surface pressure is achieved, the maximum oscillating rate is set to 3mm/min. Our target surface pressure was 22mN/m so that the deposition is implemented at the highest usable surface pressure before collapse. The gaseous phase is not resolved due to limited trough area, as shown in figure 3.9.

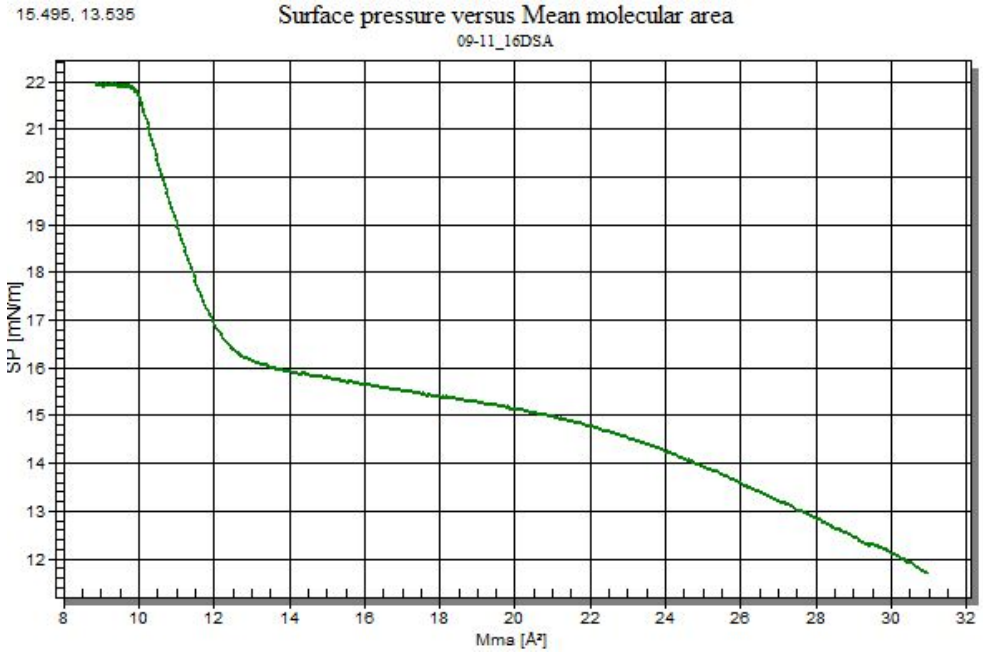


Figure 3.9: Experimental isotherm of 16-DSA on pure water with target surface pressure 22mN/m.

The floating monolayer of 16-DSA is allowed to stabilize after reaching the target surface pressure with the barriers automatically adjusting position to maintain a constant surface pressure. In figure 3.10, the surface pressure is kept at 21.9mN/m. Usually at least 10 to 20 minutes are required for the stabilization, but shorter time was used in this experiment to prevent the barriers from getting too close (the barriers will hit the limit at 62.5mm).

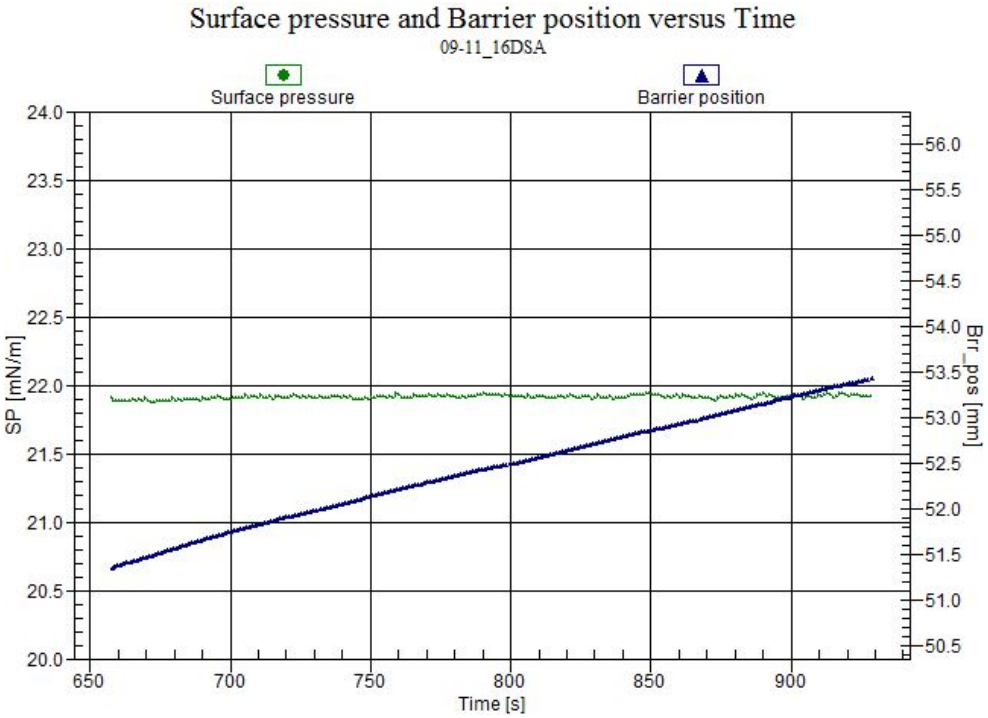


Figure 3.10: Stabilization of 16-DSA showing the change of surface pressure and barrier position over time.

The floating monolayer is transferred onto the quartz substrate at a rate of 15mm/min. There is a small drop of surface pressure due to the distortion from the movement of the substrate raising from water, and the surface pressure is then maintained at 21.7mN/m. Figure 3.11 shows that the transfer is smooth, and the transfer ratio of 1.2 is reasonably close to 1. Due to the complexity and instability of 16-DSA molecules, this transfer ratio indicates good transfer of 16-DSA to the quartz substrate. It is also shown that the change of transfer ratio corresponds to the change of surface pressure.

The diluted 16-DSA sample is deposited at 30mN/m in the same fashion with similar transfer results.

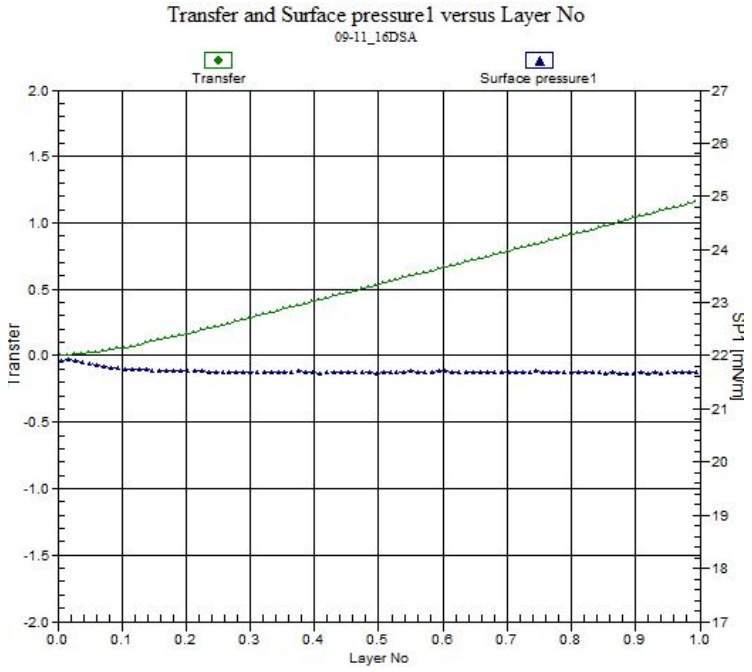


(a)

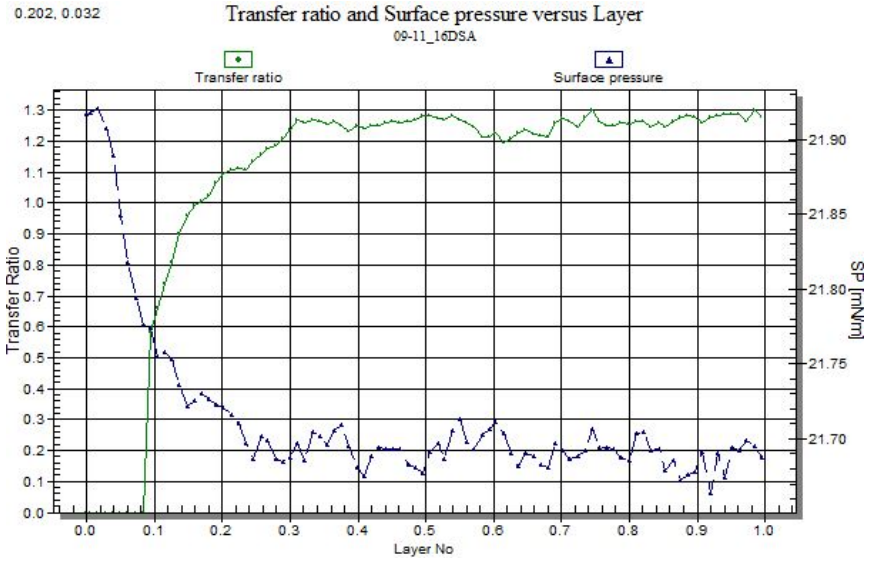


(b)

Figure 3.11: (a)Tranfer (total transfer so far) and (b) transfer ratio of 16-DSA.

# Chapter 4

# Film Characterization

To characterize the structure of the fabricated spin-labeled monolayer films, ESR and AFM measurements were performed. The ESR characterization was conducted on a Bruker EMX X-band CW ESR spectrometer operating at 9.8GHz [15].Atomic force microscopy (AFM) images were gathered in FastScan mode by Bruker FastScan AFM located in the Quantum Nanofabrication clean room (QNFCR) [**?**] and processed by NanoScope Analysis software.

## 4.1 ESR Characterization

In order to check the purchased 16-DSA quality and the sensitivity of the EMX ESR spectrometer, roughly $10^{14}$ molecules of 16-DSA in chloroform solution contained in a 3mm ESR sample tube was first measured at room temperature. All parameters were optimized to have a good SNR for film measurements, shown in table 4.1. The microwave power was set by adjusting the attenuator to have a good signal intensity without power broadening. The modulation frequency was set by the system, and the modulation amplitude was chosen as a good compromise between line resolution and good SNR. The measurement time was set to be long enough to have a good SNR through signal averaging, and the LB film samples were scanned 16 times for each orientation.

| microwave power | power attenuation | modulation frequency | modulation amplitude | sweep time | detector time constant |
|---|---|---|---|---|---|
| 2mW | 20dB | 100kHz | 2G | 200.04s | 327.68ms |

Table 4.1: Operating conditions for ESR measurements.

### 4.1.1 Measurement

The sample was scanned over a range of 3300Gauss (G) to 3400G which is appropriate for nitroxide radicals at a cavity resonance of 9.38 GHz with $g \approx 2$. A clear feature for $S = \frac{1}{2}$ and $I = 1$ hyperfine splitting is shown in figure 4.1 [5]. The peak-to-peak line-width is 2.6G, and the splitting between adjacent lines is 14.6G, consistent with literature values [1].

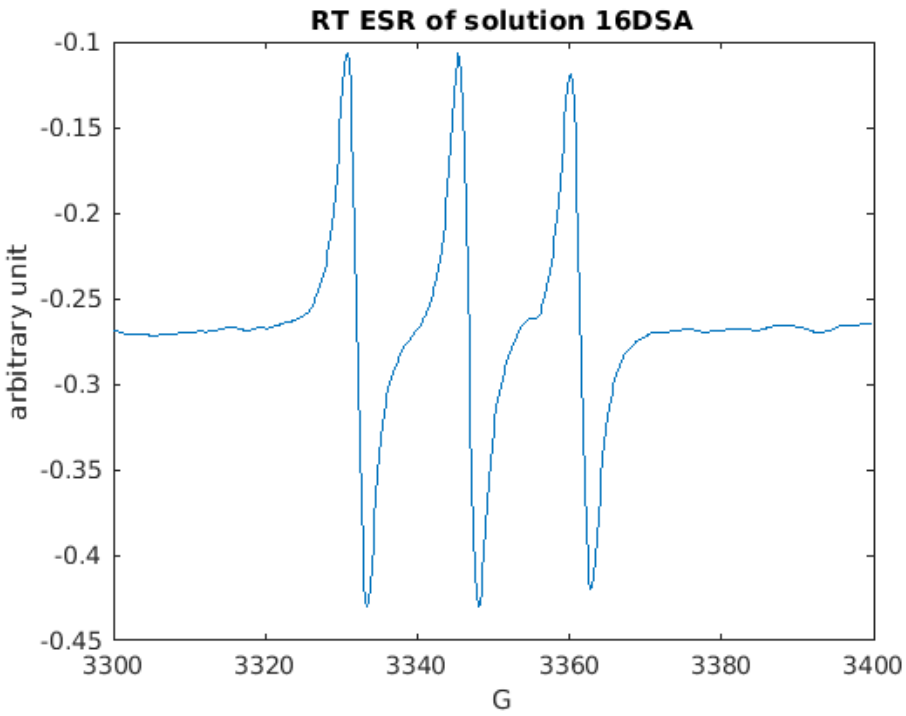


Figure 4.1: Toom temperature ESR spectrum of 16-DSA in chloroform solution measured for 3 scans under different conditions from Table 4.1.

A monolayer LB film consisting of 16-DSA was measured with different angles of the substrate norm relative to the static magnetic field ($\theta$) by placing the film in a 5mm ESR sample tube with an attached goniometer, as shown in figure 4.2. The sample was scanned over a range of 3430G to 3590G, appropriate for nitroxide radicals at the cavity resonance of 9.85 GHz. To avoid significant power broadening associated with long $T_1$ relaxation at cryogenic temperatures, measurements were performed at room-temperature. The cryostat was removed from the cavity to enable the use of larger sample tubes that easily accommodate the size of the LB substrate (3.78mm×30mm×0.5mm). Spectra were recorded in steps of 15° starting with the substrate surface oriented normal to the field ($\theta = 0°$) and ending with the substrate surface parallel with the field ($\theta = 90°$).

Figure 4.2: Goniometer setup for substrate rotation in the field.

The molecules comprising the monolayer film are bound to the substrate surface, limiting mobility. Thus, even though the measurements are performed at room temperature, and some motional averaging of spin-spin interactions occurs, it is expected that the sample behaves as a viscous liquid or a liquid crystal at non-cryogenic temperatures, requiring slow-motion analysis using the stochastic Liouville equation (SLE) [1, 30]. The computation of CW ESR spectra in this regime is rather complicated, so a standard implementation of a SLE solver (EasySpin) was used. An order parameter can be extracted by analyzing the resulting spectral fits [1]. There is small variation of resonator frequency due to the sample positioning in each measurement, so the recorded spectra were refined to locate at the resonant field corresponding to the same resonator frequency.

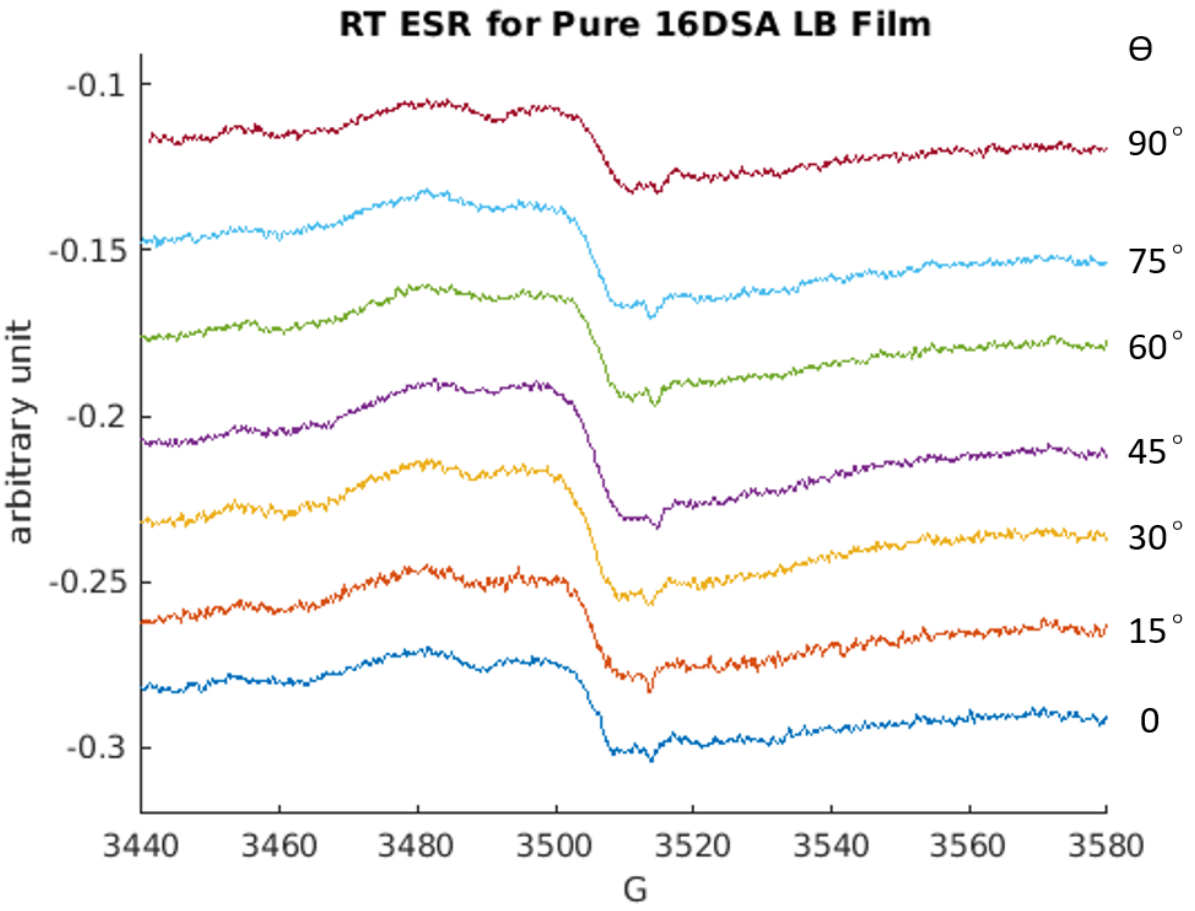


Figure 4.3: Orientation dependence of 16-DSA monolayer LB film.

A clear orientation dependent feature is revealed in figure 4.3. The line is broader than the solution 16-DSA spectrum as there is limited motional averaging. The line-width and the center field vary at different orientation, as shown in figure 4.5. The spectrum line-width is minimized when the dominant orientation distribution of sample principal axis is aligned with the magnetic field (shown in the appendix). Besides spatial averaging, Heisenberg spin exchange, electron dipole-dipole interaction, and molecular motion also contribute to the line-shape.

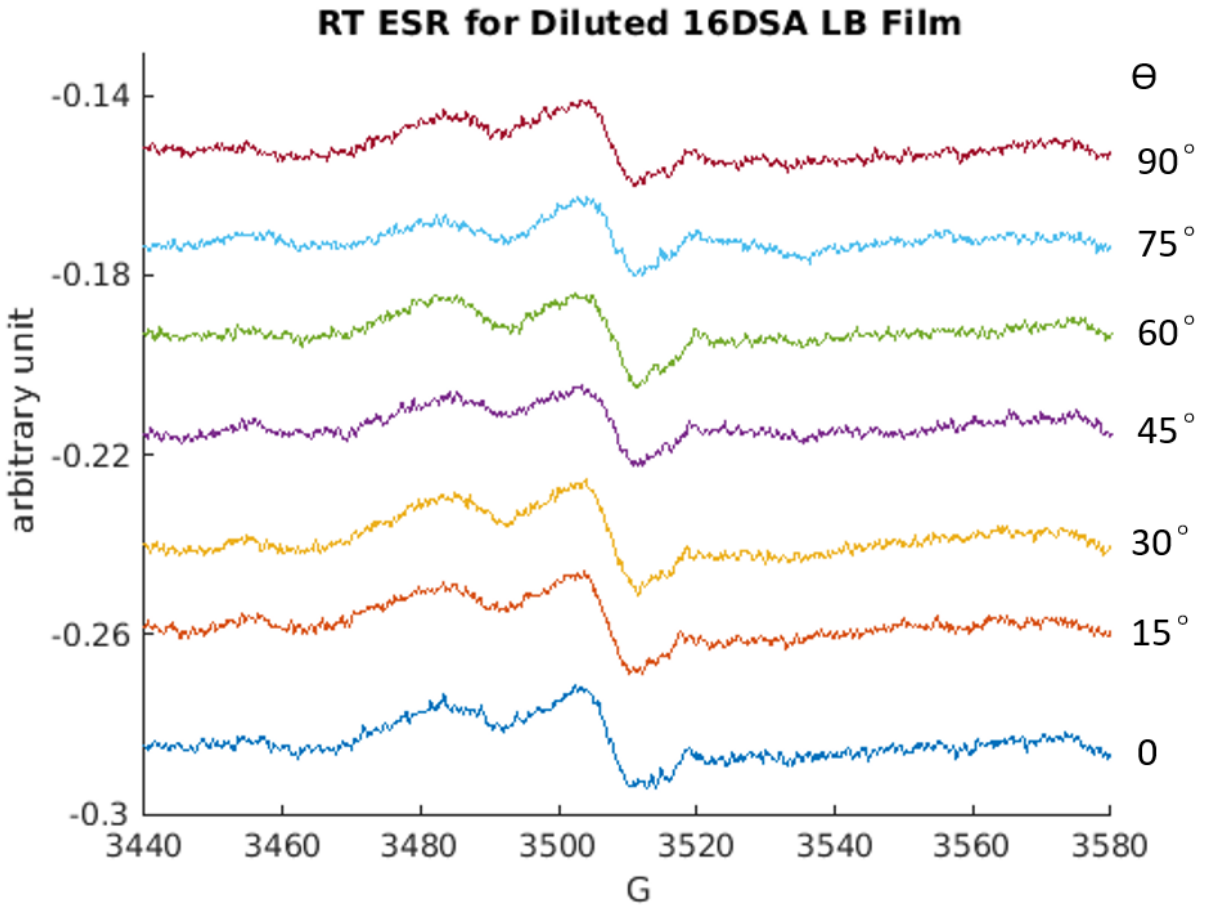


Figure 4.4: Orientation dependence of a diluted 16-DSA (1:2 16-DSA:SA) monolayer LB film.

To examine the influence of Heisenberg exchange and electron spin-spin interactions, a diluted 16-DSA film (1:2 16-DSA:SA) was measured under the same conditions as the 16-

DSA sample for comparison (figure 4.4). The Heisenberg exchange interaction and electron-electron dipolar interaction are expected to be reduced due to larger spacing between spin-labeled molecules, but a higher mobility of electrons spins is also expected. Thus, there is no strong reduction of peak-to-peak line-width, but the resonance peak is more structured and hyperfine splittings become more resolved. The SNR for both pure 16-DSA and diluted films were 30 after 16 scans (calculated from the ratio of signal intensity and standard derivation of noise). Although the signal intensity for a diluted 16-DSA film is reduced, the lineshape is also narrower, so the SNR was not largely reduced for a diluted sample.

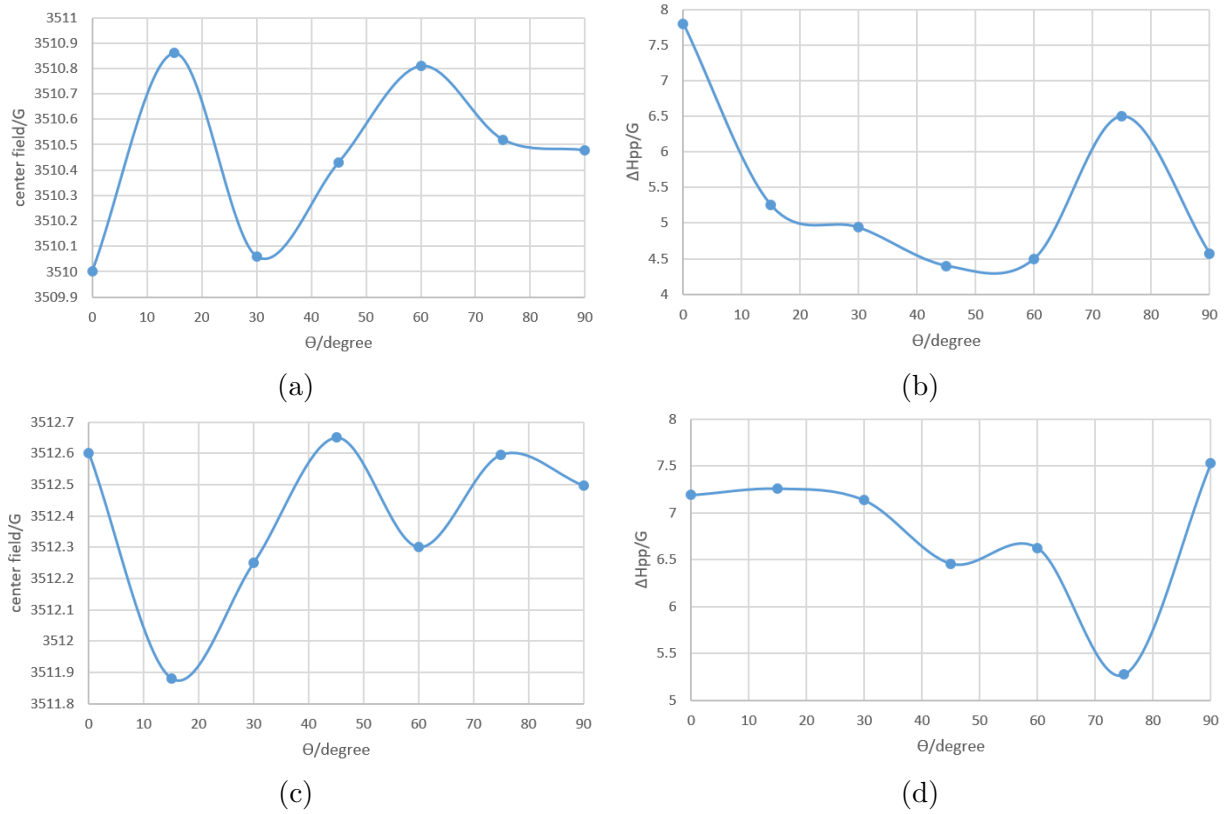


Figure 4.5: Orientation dependence of pure 16DSA: (a) center field; (b) peak-to-peak line-width; diluted 16DSA: (c) center field; (d) peak-to-peak line-width.

### 4.1.2 Sample Aging

When considering applications of the physisorbed spin-labeled monolayers, it is important to understand their stability over time. The time evolution of the 16-DSA film ESR spectrum for a single orientation ($\theta = 0°$) over the course of a week is shown in figure 4.6.

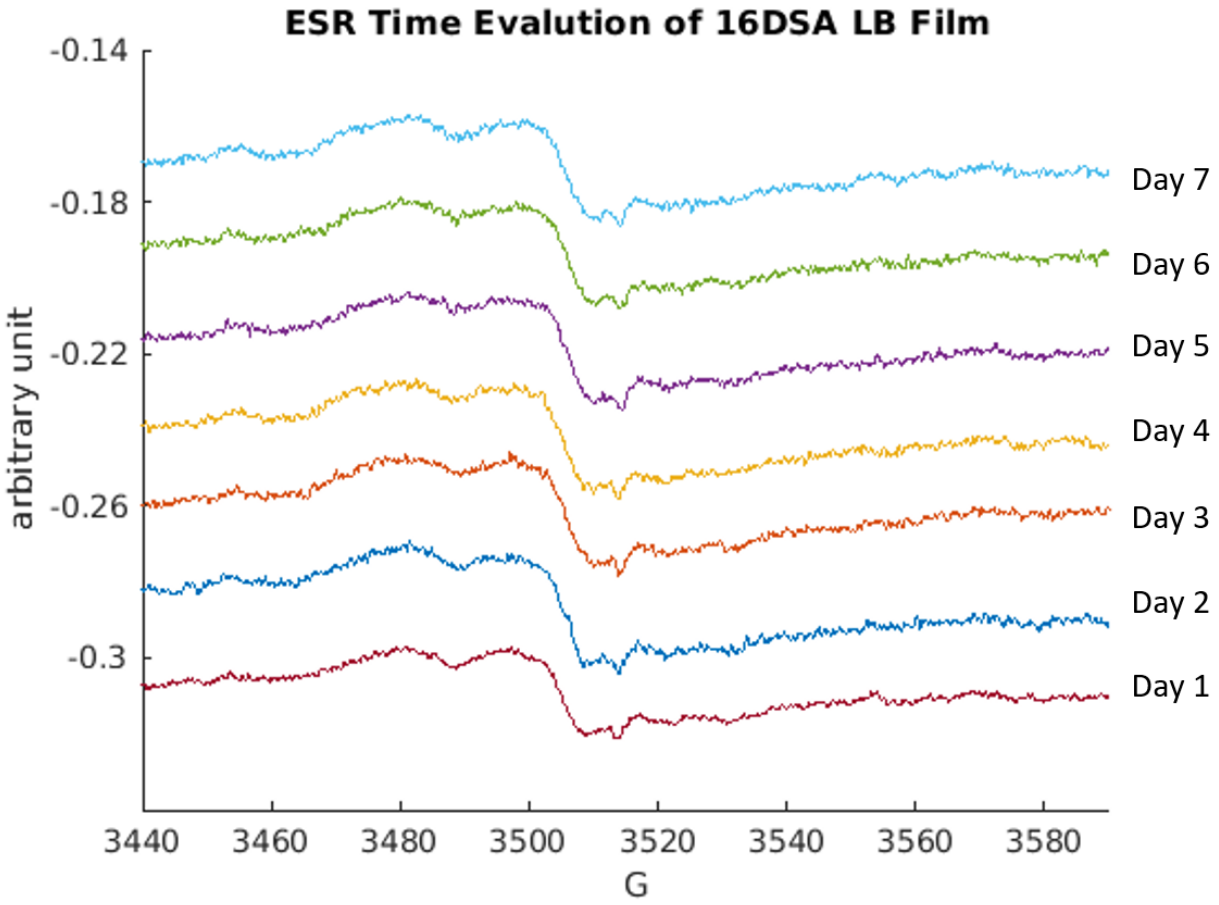


Figure 4.6: Aging of 16-DSA monolayer LB film.

Stored at room temperature, 16-DSA samples maintained good stability, showing minimal change in the spectrum. Diluted 16-DSA samples showed similar behavior and remained stable at room temperature.

## 4.2 Order Parameter

The degree of orientation order in an ESR sample can be described by an order parameter, $S$, which is defined for a liquid crystal to be the canonically weighted average value of the second order Legendre polynomial [19, 20, 1, 24]:

$$S =< P_2(\cos\theta) >= \frac{< 3\cos^2\theta - 1 >}{2}$$

A crystal with perfect order will have a value of $S = 1$, and a value of $S = 0$ indicates a structure with no order. A higher value of $S$ indicates a more ordered structure. The order parameter for biomembranes typically ranges from 0.5 to 0.7 [18]. $S$ can be calculated by a molecular tensor ($T$):

$$S = \frac{T_\parallel - T_\perp}{T_{ZZ} - \frac{1}{2}(T_{XX} + T_{YY})} \cdot \frac{a}{a'}$$

$$a = \frac{1}{3}(T_{ZZ} + T_{YY} + T_{XX})$$

$$a' = \frac{1}{3}(T_\parallel + 2T_\perp)$$

For a spin-labeled fatty acid like 16-DSA, it can be calculated from the hyperfine splitting by

$$S = \frac{T_\parallel - T_\perp - C}{T_\parallel + 2T_\perp + 2C} \cdot 1.66$$

$$C = 1.4G - 0.053(T_\parallel - T_\perp)$$

Due to line broadening of the measured LB films, exact values of hyperfine coupling parameters could not be extracted directly from the ESR spectrum. In this case, a better option is to determine $S$ through numerical simulation by fitting the experimental data to a model [2, 33].

### 4.2.1 Simulation

The line-shapes of ESR spectra of 16-DSA films were analyzed by simulation based on modulating Zeeman and hyperfine anisotropies in a slow motion regime ($10^{-9}$s< correlation time, $\tau < 10^{-7}$s) [4]. An easier simulation without considering any motion effects can be applied to low temperature (4K) measurements, but the sensitivity at low temperature was found to be insufficient to observe any signal due to power broadening from the low-temperature enhanced $T_1$ relaxation [1].

The slow-motion simulation algorithm is based on the SLE, which is given by the quantum mechanical Liouville equation describing a stationary Markov process [1]:

$$\partial\rho(\Omega,t)/\partial t = -i[\mathcal{H}(\Omega(t)),\rho(\Omega,t)] - \Gamma_\Omega\rho(\Omega,t)$$

where $\Omega \equiv \alpha,\beta,\gamma$ represents Euler angles specifying orientation, $\rho(\Omega,t)$ is the associated density matrix, $\mathcal{H}(\Omega)$ is the associated spin Hamiltonian, and $\Gamma_\Omega$ is a rotational diffusion tensor operator.

The ESR absorption spectrum can be written as

$$I(\omega) = \frac{1}{\pi} Re\langle v|[i(\omega 1 - L) + \Gamma]^{-1}|v\rangle$$

where $\Gamma$ is the symmetrized diffusion operator, $L$ is the Liouville operator associated with the Hamiltonian of the magnetic interactions, and $|v\rangle$ is the unit vector of the allowed ESR transitions in the Liouville space [6].

The Hamiltonian assuming negligible nuclear Zeeman interactions is

$$\mathcal{H} = \frac{\beta_e}{\hbar} S \cdot g \cdot B + \gamma_e S \cdot A \cdot I$$

The principal values of the $g$- and $A$- tensor for 16-DSA are [32]:

$$\begin{aligned} g_x &= 2.0088 & A_{xx}[G] &= 6.0 \\ g_y &= 2.0059 & A_{yy}[G] &= 5.7 \\ g_z &= 2.0027 & A_{zz}[G] &= 33.8 \end{aligned}$$

The matrix elements of $L$ can be calculated from the Hamiltonian written in spherical tensor notation.

For a liquid crystal, the rotational diffusion operator under a Brownian motion model is given by the symmetrized Smoluchowski equation:

$$\Gamma_\Omega = [J - \frac{1}{2k_BT}(JU)]R[J + \frac{1}{2k_BT}(JU)]$$

where $J$ is the angular momentum operator, $U$ is the mean potential acting on the molecule, and $R$ is the rotational diffusion tensor of the molecule [6].

The Boltzmann equilibrium orientation distribution probability [24] is

$$P(\Omega) = \frac{exp[-U/k_BT]}{\int exp[-U/k_BT]d\Omega}$$

The orienting potential considering only the leading term is assumed to be

$$U = -k_BT\lambda_{20}P_2(\cos\theta)$$

The order parameter is calculated by computing the integral of the normalized probability distribution:

$$S = \int_0^\pi P(\theta)\frac{(3\cos^2\theta - 1)\sqrt{5/\pi}}{4}\sin\theta d\theta$$

The spin exchange operator is assumed to be orientation independent, and the strength of it is determined by the exchange rate, $\omega$. The overall $\Gamma$ is a superposition of all relaxation processes:

$$\Gamma = \Gamma_\Omega + \Gamma_{exchange}$$

The correlation time is defined for Brownian motion as

$$\tau = \frac{1}{6D}$$

where $D$ is the rotational diffusion rate which is the principal value of the rotational diffusion tensor.

The possible spin dipole-dipole interactions give rise to isotropic line broadening, so it affects the value of motion-independent FWHM line-width $lw$ ($\frac{1}{\pi T_2}$).

The magnetic parameters obtained that gave a good fit for 16-DSA films, shown in figure 4.7, were: $\tau = 1.86 \times 10^{-8}$s, $lw = 13.4$G, $\omega = 2.49$MHz; for diluted 16-DSA films, shown in figure 4.8, the parameters were: $\tau = 8.65 \times 10^{-9}$s, $lw = 10.8$G, and the exchange rate was set to zero. For diluted 16-DSA, since the concentration of radicals is reduced, it is assumed that the spin-spin contributions including the spin exchange interaction and dipole-dipole interaction are neglected.

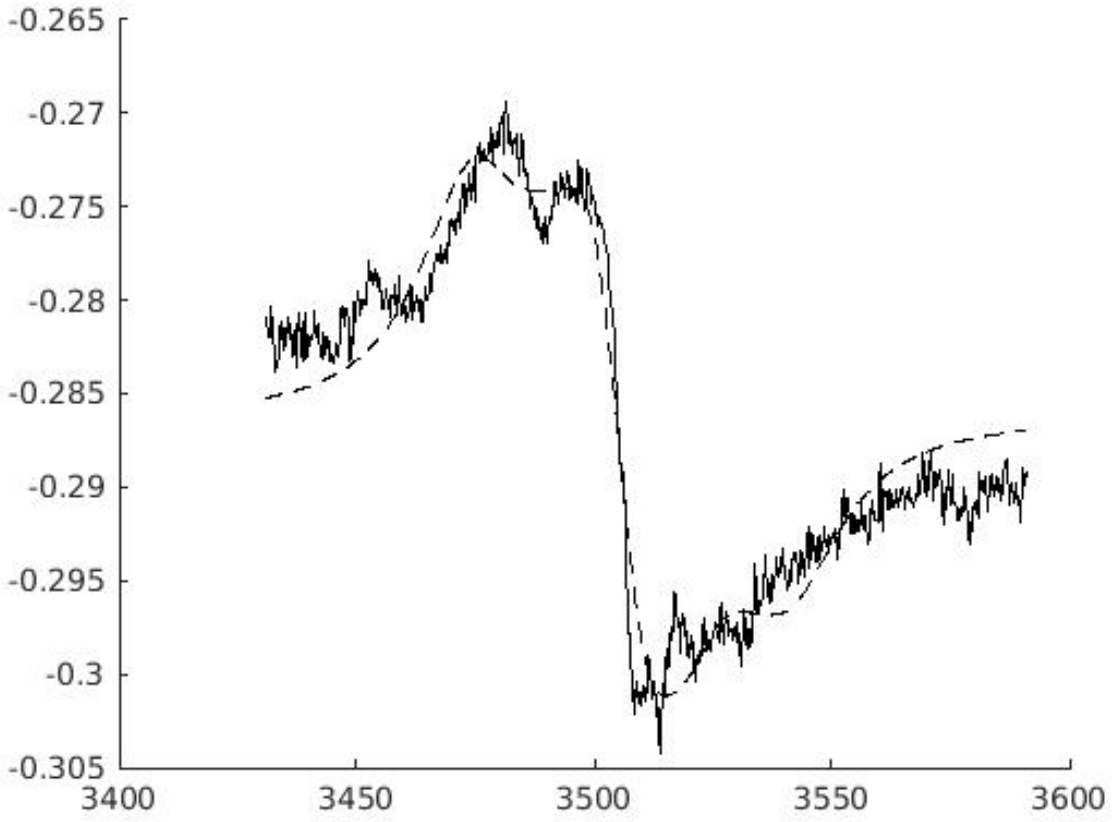


Figure 4.7: Simulation of 16-DSA monolayer LB film ($\tau = 1.86 \times 10^{-8}$s, $lw = 13.4$G, $\omega = 2.49$MHz, $S = 0.6$).

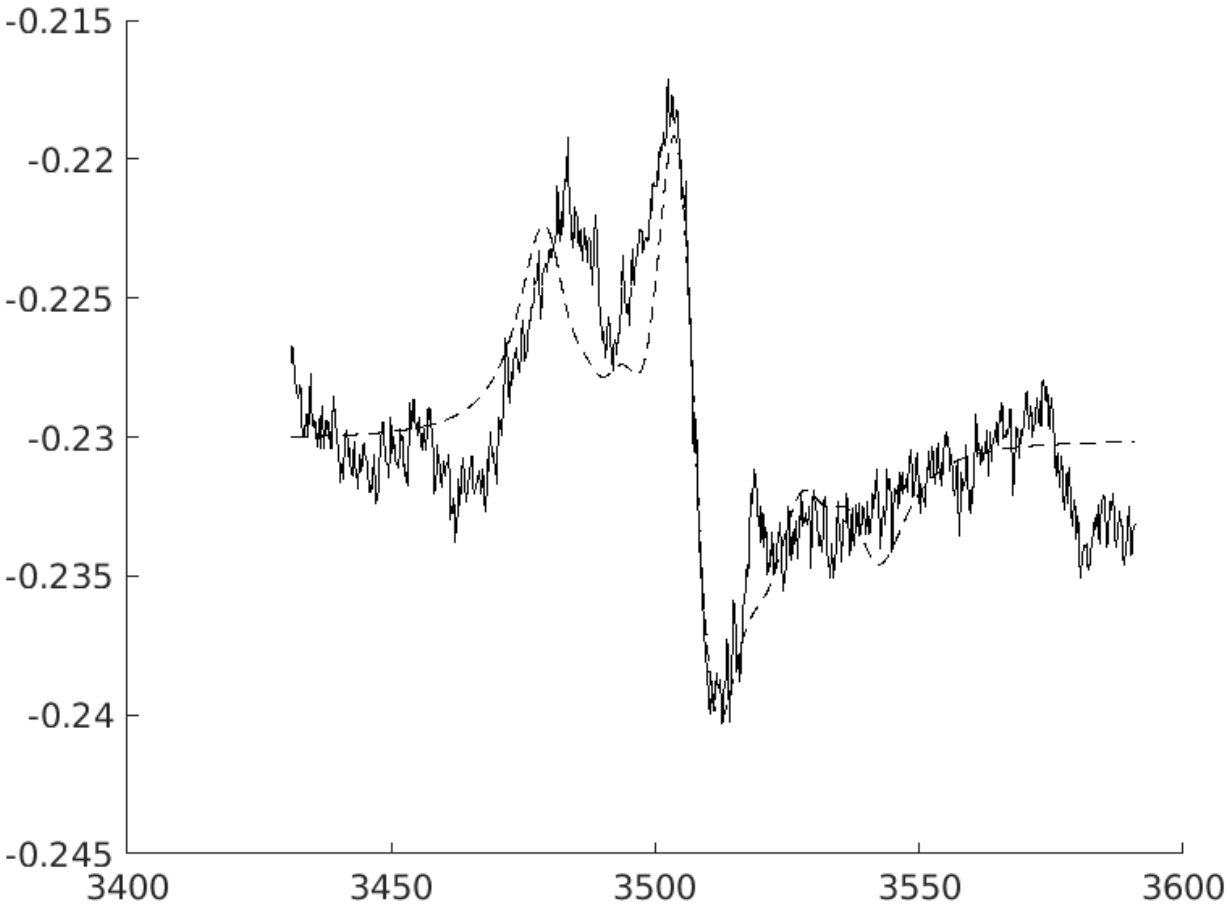


Figure 4.8: Simulation of diluted 16-DSA monolayer LB film ($\tau = 8.65 \times 10^{-9}$s, $lw = 10.8$G, $S = 0.5$).

The calculated order parameter was 0.6 for 16-DSA and 0.5 for diluted 16-DSA, suggesting that the monolayer LB film of pure 16-DSA is more ordered than the monolayer LB film of mixed 16-DSA and stearic acid. It is possible that the nitroxide groups experience more intermolecular forces in pure 16-DSA samples, which enhance the alignment of radicals when the concentration is higher.

## 4.3 AFM Characterization

A 1 $\mu$m range scan of a 16-DSA monolayer LB film, a diluted 16-DSA monolayer LB film, and a blank quartz substrate are compared in figure 4.9. The film thickness (estimated from the height of the brighter parts) is around 2.5nm, which is in good agreement with the length of a 16-DSA molecule [21].

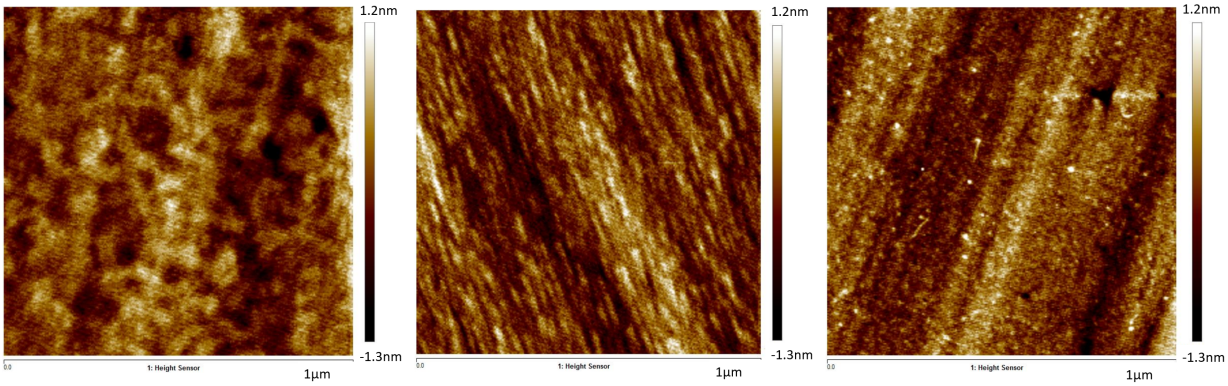


(a) (b) (c)

Figure 4.9: (a) 16-DSA monolayer on quartz substrate; (b) diluted 16-DSA monolayer on quartz substrate; (c) blank quartz substrate.

From the topographic features, it is shown that 16-DSA and stearic acid molecules are evenly distributed on the substrate. The quartz substrate is a single crystal with a very flat surface, and the films are distinguished from the substrate by patterns showing local molecular organization. The pattern domains appear to be larger for a pure 16-DSA film than a film of mixed 16-DSA and stearic acid consistent with the calculated order parameter from ESR measurements. Additionally, the shape of local patterns reveal the presence of locally ordered and disordered domains.

# Chapter 5

# Conclusions and Future Work

The fabrication as well as CW ESR and AFM characterization of monolayer LB films were presented. Monolayer films of 16-DSA and its mixture with stearic acid (1:2) were deposited on quartz substrates using a KSV NIMA Langmuir-Blodgett deposition trough. As 16-DSA is a spin-labeled fatty acid, it may be detected by ESR measurements. The spreading isotherms, the stability of floating monolayers before deposition, and the transfer plots were recorded and analyzed. The transfer ratios were close to 1, indicating good deposition of the monolayer films.

CW ESR characterization was conducted on a Bruker EMX X-band CW ESR spectrometer at room temperature. The orientation-dependent spectra of monolayer 16-DSA and diluted 16-DSA LB films containing roughly $10^{14}$ electron spins were successfully measured and recorded for the first time. The samples showed good stability even when stored at room temperature. The order parameter was 0.6 for 16-DSA films and 0.5 for diluted 16-DSA films, calculated from the spectral line-shape via numerical simulation, fitting Zeeman anisotropy, hyperfine anisotropy, correlation time, Heisenberg electron exchange, and electron dipole-dipole interaction. LB films of pure 16-DSA showed higher ordering compared to mixed films, but both showed the presence of complex structure. AFM images were also gathered on Bruker FastScan AFM as a reference of film quality.

Beyond this work, different materials should be explored for the highest ordered monolayer films. Low temperature CW ESR analysis as well as pulsed ESR experiments based on CW ESR characterization can also be studied in the future to gain further information on film structure and investigate the potential for novel applications in biological imaging and quantum information science.

# References


[1] Lawrence J. Berliner. *Spin Labeling: Theory and Applications*. Academic Press, Inc, New York, New York, 1976.

[2] Harden M. McConnell Betty Jean Gaffney. The paramagnetic resonance spectra of spin labels in phospholipid membranes. *Journal of Magnetic Resonance*, 16(1):1–28, 1969.

[3] Troy Borenman. Techniques for noise suppression and robust control in spin-based quantum information processors. *Thesis (Ph. D.)–Massachusetts Institute of Technology*, 74(11):B, 2013.

[4] Giacomo Martini Francesca Bonosi, Gabriella Gabrielli and M. Francesca Ottaviani. Monolayers and langmuir-blodgett films of doxylstearic acids. spreading isotherms and esr study. *Langmuir*, 5(4):1037–1043, 1989.

[5] Ian Gentle Geoffrey Barnes. *Interfacial Science: An Introduction*. Oxford University Press Inc, New York, New York, 2005.

[6] Rebecca Pogni Giovanni Della Lunga and Riccardo Basosi. Computer simulation of epr spectra in the slow-motion region for copper complexes with nitrogen ligands. *J. Phys. Chem.*, 98(15):3937–3942, 1994.

[7] M.F.Ottaviani G.Martini, F.Bonosi and G.Gabrielli. Langmuir-blodgett films of pure long-chain nitroxides, their mixtures and mixtures with stearic acid studied by electron spin resonance. *Thin Solid Films*, 178(1-2):271–279, 1989.

[8] Marcus A. Hemminga and Lawrence J. Berliner. *ESR Spectroscopy in Membrane Biophysics*. Springer Science+Business Media, LLC, New York, New York, 2007.

[9] James R. Bolton John A. Weil. *Electron paramagnetic resonance: elementary theory and practical applications*. John Wiley and Sons, Inc, Hoboken, New Jersey, second edition, 2007.

[10] Imma Ratera Concepcio Rovira Judith Guasch, Xavier Fontrodona and Jaume Veciana. The perchlorotriphenylmethyl (ptm). *Langmuir*, 15(10):3551–3556, 1999.

[11] Masamichi Fujihira Kosaku Suga, Yutaka Iwamoto. Characterization of polyion complexed langmuir-blodgett films by electron spin resonance. *Thin Solid Films*, 243(1-2):634–637, 1994.

[12] Yang Leng. *Materials Characterization: Introduction to Microscopic and Spectroscopic Methods, Second Edition*. Wiley-VCH Verlag GmbH and Co. KGaA, Weinheim, second edition, 2013.

[13] W. RBarger M. D. Pace and A. W. Snow. Epr of copper tetrakis(cumylphenoxy)phthalocyanine langmuir-blodgett films. *Journal of Magnetic Resonance*, 75(1):73–82, 1987.

[14] Xinhua Chen Maurizio Romanelli, Francesca Bonosi and Larry Kevan. Electron spin echo of a langmuir-blodgett film. *Langmuir*, 7(6):1039–1041, 1991.

[15] mit. Training for the bruker emx epr spectrometer.

[16] KSV NIMA. Ksv nima monolayer kit.

[17] KSV NIMA. Ksv nima software manual.

[18] Marvin D. Kemple Richard A. Haak Frederick W. Kleinhans Norman D. Lees, Martin Bard. Esr determination of membrane order parameter in yeast sterol mutants. *Biochimica et Biophysica Acta (BBA) - Biomembranes*, 553(3):469–475, 1979.

[19] Michael Hird Peter J. Collings. *Introduction to Liquid Crystals: Chemistry and Physics*. Taylor and Francis Ltd, London, 1997.

[20] Michael C. Petty. *Langmuir-Blodgett Films: An Introduction*. Press Syndicate of The University of Cambridge, Cambridge, 1996.

[21] Akira Fujishima Phillip Sawunyama and Kazuhito Hashimoto. Photocatalysis on tio2 surfaces investigated by atomic force microscopy: Photodegradation of partial and full monolayers of stearic acid on tio2(110). *Langmuir*, 15(10):3551–3556, 1999.

[22] Charles P. Poole. *Electron Spin Resonance : A Comprehensive Treatise on Experimental Techniques*. Interscience Publishers, New York, New York, second edition, 1983.

[23] Philip H Rieger. *Electron Spin Resonance: Analysis and Interpretation*. The Royal Society of Chemistry, Cambridge, 2007.

[24] Shulamith Schlick. *Advanced ESR Methods in Polymer Research*. John Wiley and Sons, Inc, Hoboken, New Jersey, 2006.

[25] Daniella Goldfarba Sharon Ruthstein, Reit Artzi and Ron Naaman. Epr studies on the organization of self-assembled spin-labeled organic monolayers adsorbed on gaas. *Physical Chemistry Chemical Physics*, 7(3):524–529, 2005.

[26] Shin-ichiKuroda. Characterization of langmuir—blodgett films using electron spin resonance spectroscopy. *Colloids and Surfaces A: Physicochemical and Engineering Aspects*, 72(17):127–141, 1993.

[27] Shin-ichiKuroda. Electron spin resonance characterization of langmuir–blodgett films containing functional molecules. *Colloids and Surfaces A: Physicochemical and Engineering Aspects*, 198-200(18):735–744, 2002.

[28] Sigma-Aldrich. 16-doxyl-stearic acid, free radical.

[29] Sigma-Aldrich. Stearic acid.

[30] Arthur Schweiger Stefan Stoll. Easyspin: Simulating cw esr spectra. *Biological Magnetic Resonance*, 27:299–321, 2007.

[31] R. Barghout R. G. Compton D. J. Riley T. Richardson, G. G. Roberts. Langmuir–blodgett films of doxyl-stearic acids: Cyclic voltammetry. *Electroanalysis*, 3(8):757–762, 1991.

[32] J. Schmidt G. Abend H. Hamann T. Risse, T. Hill and H. J. Freund. Investigation of the molecular motion of self-assembled fatty acid films. *The Journal of Physical Chemistry B*, 102(15):2668–2676, 1998.

[33] A. Yu. Bobrovsky T. S. Yankova and A. Kh. Vorobiev. Order parameters p2, p4, and p6 of aligned nematic liquid-crystalline polymer as determined by numerical simulation of electron paramagnetic resonance spectra. *The Journal of Physical Chemistry B*, 116(20):6010–6016, 2012.

[34] Transformative Quantum Technologies. Lab equipment photos [hq].

# APPENDICES

# Appendix A

# Mathematica Notebook

## A.1 PTM Simulation

The ESR spectra of PTM can be fitted by simulation of a Lorentzian function derived from Bloch equation.

```
ImportBrukerCWData[filename_] := Module
[{rawdata= Import[filename, "Data"], rawmetadata
= Import[filename <> ".DSC"], data, fields},
data = Rest@Rest@rawdata;
data = Map[Internal`StringToDouble, Flatten@*StringSplit /@ data, {2}];
fields = data[[All, 2]];
data = data[[All, 3]];
Transpose[{fields, data}]]

nlm = NonlinearModelFit[data1,
  c + A*(2*\[Pi]*g*9.27401*10^-28*B0/(6.62607*10^-34) -
       2 \[Pi] 9.386*10^9)/(1 +
       T2^2*(2*\[Pi]*g*9.27401*10^-28*B0/(6.62607*10^-34) -
          2 \[Pi] 9.386*10^9)^2)^2, {{A, 1}, {g, 2}, {T2,
    10^-8}, {c, -0.5}}, B0];
nlm["ParameterTable"]
Normal[nlm]
```

```
Show[ListPlot[data, PlotRange -> All],
 Plot[nlm[B], {B, 3300, 3400}, PlotRange -> All]]
```

The simulation gives a change of effective g factor (shown below) which indicates the orientation dependence of Zeeman splitting of a crystallized sample.

| rotation angle | 0 | $\pi/4$ | $\pi/2$ |
|---|---|---|---|
| g factor | 2.00037 | 2.00177 | 2.00091 |

Table A.1: Effective g factors.

## A.2 Simulation of A Partially Ordered Crystal

A partially ordered crystal sample will show the sharpest ESR signal when the dominant orientation distribution of sample principal axis is aligned with the magnetic field. An example based on g- anisotropy for a rotation of $\theta$ with the orientation distribution centered at $\theta = \pi/3$ is shown below:

```
 geff[gx_, gy_, gz_, \[Theta]_, \[Phi]_ ] =
  With[{g = (EulerMatrix[{0, 0,
         0}].EulerMatrix[{0, \[Theta], \[Phi]}].DiagonalMatrix[{gx,
         gy, gz}].EulerMatrix[{0, \[Theta], \[Phi]}]\
\[ConjugateTranspose].EulerMatrix[{0, 0, 0}]\[ConjugateTranspose])},
   Sqrt[g[[3, 1]]^2 + g[[3, 2]]^2 + g[[3, 3]]^2]];
sig[gx_, gy_, gz_, \[Theta]_, \[Phi]_, Bmin_, Bmax_, dB_, \[Nu]_, T2_,
    A1_] := Table[
   Module[{E = 1.399625 B geff[gx, gy, gz, \[Theta], \[Phi] ]},
    A1 T2/(1 + T2^2 4 \[Pi]^2 ( E - \[Nu])^2 ) ] , {B, Bmin, Bmax,
    dB}];
avesig[gx_, gy_, gz_, Bmin_, Bmax_, d\[Theta]_, d\[Phi]_, dB_, \[Nu]_,
    T2_, A1_] :=
  Sum[sig[gx, gy, gz, \[Theta], \[Phi], Bmin, Bmax, dB, \[Nu], T2,
     A1] Exp[-((\[Theta] - \[Pi]/6)/(\[Pi]/24))^2/
       2 - ((\[Phi] - \[Pi]/2)/(\[Pi]/12))^2/2] Abs[
     Sin[\[Theta]]] d\[Theta] d\[Phi] , {\[Theta], 0, \[Pi]/3,
```

```
    d\[Theta]}, {\[Phi], \[Pi]/6, 5 \[Pi]/6, d\[Phi]}];
spectrum =
  avesig[2.0029, 2.0013, 1.9974, 3346, 3361, 0.105/8, 0.105/16, 0.05,
   9386, 0.35, 333];
data = Transpose[{Table[i, {i, 3346, 3361, 0.05}], spectrum}];
derivdata =
  Transpose[{Table[i, {i, 3346, 3361, 0.05}][[;; -2]],
    Differences[spectrum]}];
ListPlot[derivdata, PlotRange -> All, Joined -> True]
```

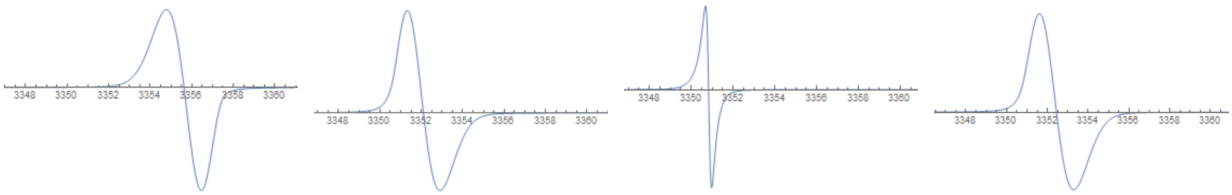


(a) (b) (c) (d)

Figure A.1: ESR signal with a rotation of: (a) $\theta = 0$; (b) $\theta = \pi/6$; (c) $\theta = \pi/3$; (d)$\theta = \pi/2$.

As shown in figure A.1, the ESR signal is the sharpest when the dominant orientation $\theta = \pi/3$ is aligned with the magnetic field.

# Appendix B

# Procedure for Monolayer LB Film Fabrication

This procedure describes detailed steps of depositing a monolayer film on a hydrophilic substrate.

## B.1 Preparation

### B.1.1 Sample Preparation

1. Weigh an empty sample vial.

2. Weigh some monolayer material in the weighted vial.

3. Add chloroform to make a spreading solution with concentration of the amphiphiles around 0.5-1mg/mL.

### B.1.2 Substrate Cleaning

1. Rinse several glass beakers with acetone and ethanol.

2. Fill a beaker with toluene and place the substrate inside, then sonicate for 10 minutes. Repeat this step with acetone, ethanol, and water.

3. Remove the substrate from the beakers and place on a piece of KimWipe tissue, blow dry the substrate with a nitrogen gun.

### B.1.3 Trough System Cleaning

1. Rinse the trough system, including the barriers, the trough, the sample clamp, and the aspiration tip, with ethanol and Milli-Q water, dry with KimWipe tissues.

2. Use a piece of parafilm wax to fix a clean 1mL pipette tip to the aspirator tip.

### B.1.4 Subphase Aspiration

1. Fill the trough with 80mL Milli-Q water (such that the subphase surface is a couple of mm above the edges of the trough).

2. Rinse the polished rod with ethanol and water. Hang the rod on the surface balance.

3. Turn on the PID stage controller, turn off the isolation chamber fan.

4. Zero the balance and barrier positions from the software Manual Control Unit. Close the barriers to the center and aspirate the subphase surface simultaneously until the barriers are maximally closed. Open the barriers to the zero position and repeat this step 2-3 times. The subphase surface is considered as clean if the surface pressure value stays below 0.2-0.3 mN/m during the compression.

### B.1.5 Substrate Mounting

1. Place the substrate in the dipper sample clip holder, and attach this holder to the dipper arm. The substrate should be placed parallel with the barriers, which is shown to produce the best quality LB films.

2. Lower the substrate using the software Manual Control Unit until it just touches the subphase surface.

3. Zero the Dipper position and further lower the substrate down to the depth of the substrate desired to be coated. This height lowered is used to calculate the quality of transfer (TR) during the measurement.

### B.1.6 Sample Solution Deposition

1. Clean a syringe by placing the needle in a beaker filled with chloroform, fill and empty the syringe 5-6 times.

2. Heavily shake the sample solution bottle, take about 10$\mu$L of sample solution if its concentration is around 1mg/mL using the cleaned syringe.

3. Zero the balance and barrier positions. Spread the monolayer sample solution on the subphase by first forming a small drop of the solution on the needle tip and carefully make the drop touch the subphase surface. This should be done slowly enough that the surface pressure value does not exceed 0.5mN/m. Allow the solvent evaporate for at least 10 minutes before starting the experiment.

## B.2 Experiment Running

1. Fill the Experimental Setup and press Start.

2. Set all the parameters on Trough Controls and press Go/Hold.

3. When the target surface pressure is reached, wait for at least 10-20 minutes for the monolayer to stabilize.

4. Define the lower limit by pressing Set in Dipper Controls, and put the upper limit to 2mm to completely raise the substrate above the surface. Keep the deposition speeds around 5-10 mm/min for smooth transfer, press Start.

5. Clean the trough system after finishing experiments.